

# Excellence in Chemistry Research

## Announcing our new flagship journal

- Gold Open Access
- Publishing charges waived
- Preprints welcome
- Edited by active scientists



## Meet the Editors of *ChemistryEurope*



**Luisa De Cola**

Università degli Studi  
di Milano Statale, Italy



**Ive Hermans**

University of  
Wisconsin-Madison, USA



**Ken Tanaka**

Tokyo Institute of  
Technology, Japan

# A Combined XPS and Computational Study of the Chemical Reduction of BMP-TFSI by Lithium\*\*

K. Forster-Tonigold<sup>+, \* [a, b]</sup>, F. Buchner<sup>+, [c]</sup>, J. Bansmann<sup>, [d]</sup>, R. J. Behm<sup>, [a, c]</sup> and A. Groß<sup>[a, c]</sup>

Employing density functional theory (DFT) calculations and X-ray photoelectron spectroscopy (XPS), we identify products of the reaction of the ionic liquid *N,N*-butylmethylpyrrolidinium bis(trifluoromethylsulfonyl)imide (BMP-TFSI) with lithium in order to model the initial chemical processes contributing to the formation of the solid electrolyte interphase in batteries. Besides lithium oxide, sulfide, carbide and fluoride, we find

lithium cyanide or cyanamide as possible, thermodynamically stable product in the Li-poor regime, whilst  $\text{Li}_3\text{N}$  is the stable product in the Li-rich regime. The thermodynamically controlled reaction products as well as larger fragments of TFSI persisting due to kinetic barriers could be identified by a comparison of experimentally and computationally determined core level binding energies.

## Introduction

Besides the individual components and actual materials employed in batteries, the interface between the electrode and the electrolyte has a crucial impact on the function of the battery. Due to its interaction with the (electrified) electrode surface, the electrolyte is prone to decomposition, leading to the formation of the so-called solid electrolyte interphase (SEI).<sup>[1]</sup> Once formed and thick enough, the SEI prevents further electrolyte consumption due to the insulating nature of its constituents. Still, the SEI should be permeable for ion diffusion. Thus, the composition of the SEI crucially contributes to the function of a battery, and its detailed knowledge is of utmost importance for the functional understanding. Owing to the complexity of battery systems and because many analytical methods are not applicable for (in situ) studies of electrochemical systems, there is a demand for studies on well-defined model systems in order to understand the interactions and reactions at different interfaces.

In recent years, the use of ionic liquids (ILs) as electrolytes has attracted increasing attention.<sup>[2–4]</sup> Ionic liquids, which are defined as salts with a melting point lower than 100 °C, offer a variety of advantages, including an enhanced electrochemical stability. Nevertheless, there are reports that ILs decompose at low electrode potentials.<sup>[5–7]</sup> One of the most studied ILs is *N,N*-butylmethylpyrrolidinium bis(trifluoromethylsulfonyl)imide (BMP-TFSI).

Despite of numerous model studies on the formation of the SEI<sup>[8–12]</sup> and in particular of BMP-TFSI<sup>[13–18]</sup> in the past few years, neither the actual composition of the SEI nor the mechanisms of its formation are fully clear yet, in particular not on a molecular scale. Different decomposition products have been deduced from X-ray photoelectron spectroscopy (XPS) experiments studying the interaction of  $\text{Li}^0$  with a BMP-TFSI monolayer on graphite<sup>[15]</sup> and from XPS experiments studying the interaction of  $\text{Li}^0$  with BMP-TFSI mono- or multilayers on various oxide surfaces ( $\text{Co}_3\text{O}_4$ ,  $\text{CoO}$ ).<sup>[17,18]</sup> XPS measurements on the interaction of the IL monolayer with graphite (HOPG) suggested, that decomposition mainly affects the anion, as the N 1s peak of TFSI declines. In contrast, on oxide surfaces mainly the N 1s XPS peak of BMP was found to decline, indicating a predominant decomposition of the cation. Olschewski et al. also reported a predominant cation decomposition upon deposition of BMP-TFSI on metallic  $\text{Li}^0$ .<sup>[9]</sup> To shed more light on this apparent discrepancy and the role of the substrate, we performed a detailed study of the interactions and reactions of  $\text{Li}^0$  with BMP-TFSI multilayers on an HOPG substrate, employing a combined experimental and computational approach. Exploring the multilayer regime allows us to probe the interaction between the IL and Li without interfering interactions with the substrate. To the best of our knowledge there is no systematic study so far on the decomposition and the formation of different possible products for varying Li:IL ratios employing electronic structure methods. Previous computational studies mainly used ab initio molecular dynamics to study the decomposition of (BMP-)TFSI at lithium surfaces.<sup>[19–22]</sup> In these studies different decomposition products were found, including large fragments, such as  $\text{NSO}_2\text{CF}_3$ ,<sup>[19,20,22]</sup> but also solely atomic

[a] Dr. K. Forster-Tonigold,<sup>+</sup> Prof. Dr. R. J. Behm, Prof. Dr. A. Groß  
Helmholtz Institute Ulm (HIU) Electrochemical Energy Storage,  
Helmholtzstraße 11, 89081 Ulm, Germany  
E-mail: katrin.tonigold@kit.edu

[b] Dr. K. Forster-Tonigold<sup>+</sup>  
Karlsruhe Institute of Technology (KIT), P.O. Box 3640, 76021 Karlsruhe,  
Germany

[c] Dr. F. Buchner,<sup>+</sup> Prof. Dr. R. J. Behm, Prof. Dr. A. Groß  
Institute of Theoretical Chemistry, Ulm University, Albert-Einstein-Allee 11,  
89081 Ulm, Germany

[d] Dr. J. Bansmann  
Institute of Surface Science and Catalysis, Ulm University, Albert-Einstein-  
Allee 47, 89069 Ulm, Germany

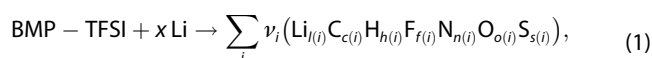
[<sup>+</sup>] These authors contributed equally.

[\*\*] A previous version of this manuscript has been deposited on a preprint server (<https://doi.org/10.26434/chemrxiv-2022-mpb1w>).

Supporting information for this article is available on the WWW under <https://doi.org/10.1002/batt.202200307>

© 2022 The Authors. Batteries & Supercaps published by Wiley-VCH GmbH. This is an open access article under the terms of the Creative Commons Attribution Non-Commercial License, which permits use, distribution and reproduction in any medium, provided the original work is properly cited and is not used for commercial purposes.

constituents,<sup>[21]</sup> depending on the length of the simulation. In the present study we use both density functional theory (DFT) calculations and X-ray photoelectron spectroscopy (XPS) to elucidate possible products of the reaction



where the stoichiometry on the right-hand side reflects the atomic constituents of BMP-TFSI.

We first present and discuss the results of systematic XPS measurements on the interaction of a multilayer film of molecularly adsorbed BMP-TFSI on an HOPG substrate with increasing amounts of metallic Li evaporated on top of it (section Experimental Results). Next we apply DFT calculations to explore the thermodynamic stability of possible decomposition products and kinetic barriers for their formation (section Thermodynamic stability of possible reaction products of BMP-TFSI and Li<sup>0</sup> and section Kinetic stability of intermediate products of the reaction of TFSI<sup>-</sup> and Li<sup>0</sup>). Subsequently, we compute core level binding energies of probable reaction products and compare these with the experimental findings in the XPS experiments to unambiguously identify the products and long-living intermediates resulting from this reaction (section Calculated core level binding energies and comparison to experiment). Finally, the results are shortly summarized and final conclusions are drawn (section Conclusion). Experimental and computational details are summarized in the Methods section at the end.

## Results and Discussion

### Experimental Results

**Multilayer peak positions and shifts vs. monolayer:** To begin with, we will summarize the XP core level peaks observed for a molecularly adsorbed BMP-TFSI multilayer film on HOPG at room temperature (r.t.) (thickness ca. 10 monolayers) (Figures 1 and 2, bottom of each panel). A molecular representation of BMP-TFSI is shown on top of Figure 1. The binding energies (BEs) of all BMP-TFSI peaks are listed in Table 1, using typical abbreviations such as C<sub>BMP/alkyl</sub>, C<sub>BMP/hetero</sub>, N<sub>BMP</sub> and C<sub>TFSI</sub>, N<sub>TFSI</sub>, F<sub>TFSI</sub>, O<sub>TFSI</sub>, S<sub>TFSI</sub> for the atoms of the BMP cation and of the TFSI anion, respectively (see our previous publications<sup>[16,23]</sup>). Regarding the C 1s BEs of the cation we distinguish between the carbon atoms in the alkyl chain or ring (C<sub>BMP/alkyl</sub>) and the carbon atoms adjacent to the N atom (C<sub>BMP/hetero</sub>).

The BEs shown in Table 1 include N 1s peaks at 403.3 and 400.0 eV, which are related to the N atoms in the BMP cation and in the TFSI anion, respectively. For comparison, we had reported BEs of 402.6 and 399.5 eV for a monolayer film adsorbed on HOPG.<sup>[15]</sup> A comparable BE up-shift, here by around 1 eV, was observed by Cremer et al.<sup>[24]</sup> when going from submono- to multilayer IL films on Au(111), which they explained by either an initial state effect, due to a bonding mechanism, or by a final state effect, due to more efficient

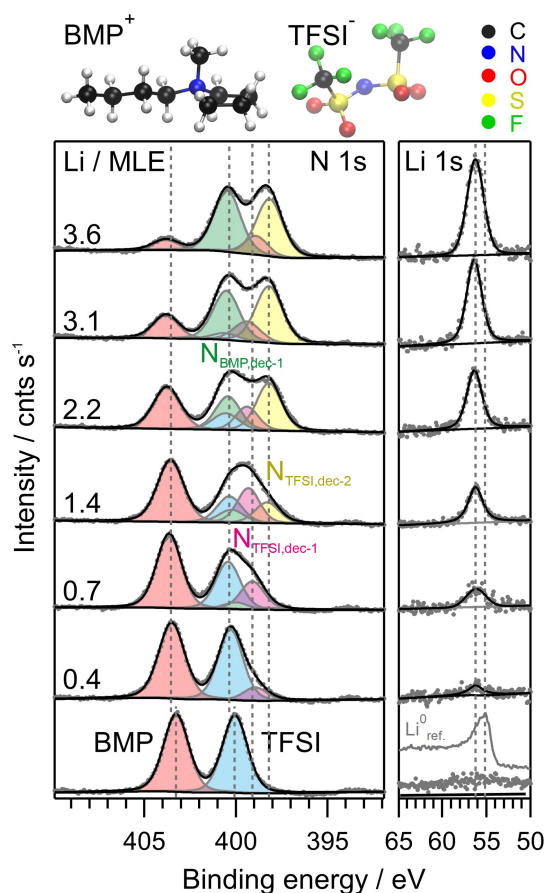


**Figure 1.** N 1s and Li 1s core level spectra of around 10 ML of molecularly adsorbed BMP-TFSI species (bottom of the N 1s region) and after stepwise post-deposition of 0.4 - 3.6 MLE of Li at r.t. For comparison, a reference spectrum for metallic Li is included in the Li 1s range.

**Table 1.** Binding energies of different XPS peaks for an adsorbed BMP-TFSI multilayer on HOPG. Abbreviations as given in the right column will be used to refer to peaks in all following XP spectra.

Element/orbital	BE [eV]	Chemical environment	denoted as
C 1s	286.0	-C-C-	C <sub>BMP/alkyl</sub>
C 1s	287.3	-C-N-	C <sub>BMP/hetero</sub>
N 1s	403.3	-C-N-	N <sub>BMP</sub>
C 1s	293.5	-C-F <sub>3</sub>	C <sub>TFSI</sub>
N 1s	400.0	-S-N-	N <sub>TFSI</sub>
F 1s	689.6	-C-F <sub>3</sub>	F <sub>TFSI</sub>
O 1s	533.3	-SO <sub>2</sub> -	O <sub>TFSI</sub>
S 2p <sub>3/2</sub>	169.6	-SO <sub>2</sub> -	S <sub>TFSI</sub>

screening of the core hole for the monolayer film. Using a similar type, but slightly different IL, Biedron et al. reported comparable findings, with an up-shift by about 0.9 eV from a submonolayer to a thick film. Based on a comparable decrease of the work function, these authors assigned this shift to a vacuum level pinning effect,<sup>[25]</sup> where the BEs of the weakly bound adsorbate are coupled to the vacuum level rather than to the Fermi level.<sup>[26,27]</sup> Considering the identical magnitude of the decrease in work function and of the up-shift in BE when going from submonolayer to thick IL films, we favor the latter explanation of the shift (vacuum level pinning). The peaks due

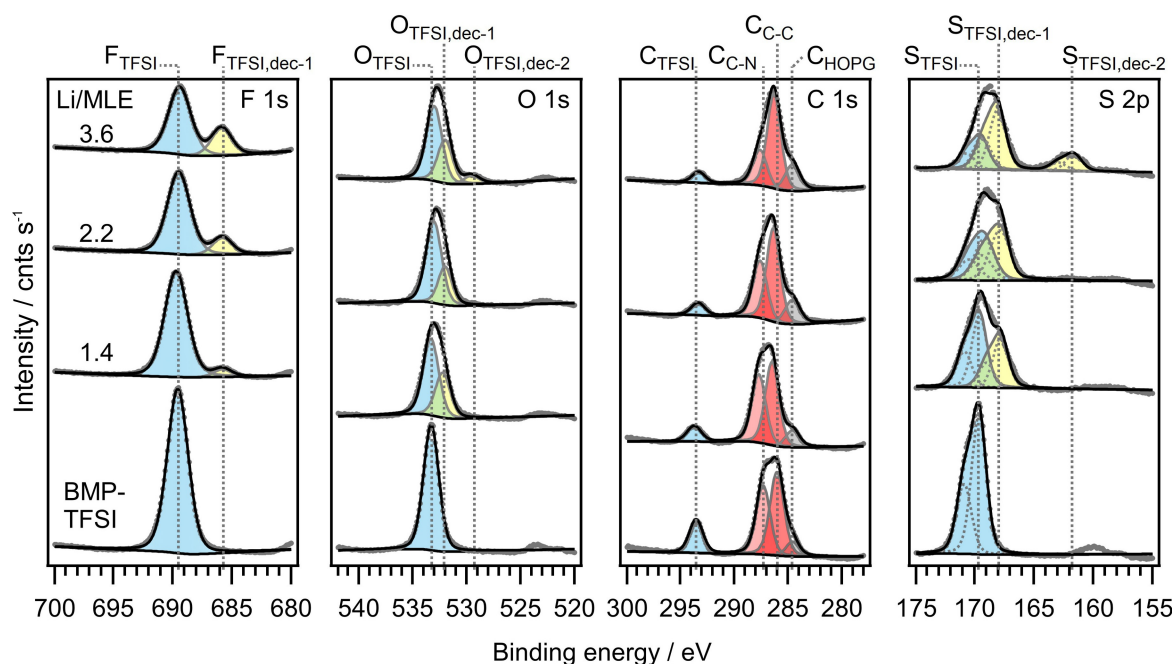


**Figure 2.** F 1s, O 1s, C 1s and S 2p core level spectra of an adsorbed BMP-TFSI multilayer ( $\sim 10$  ML) and after stepwise post-deposition of 1.4, 2.2 and 3.6 MLE of Li at r.t.

to core electrons of the other elements (see Table 1) are also up-shifted compared to the monolayer film, by about  $0.6 \pm 0.1$  eV,<sup>[23]</sup> as expected for vacuum level pinning. The intensities of these peaks (corrected by their sensitivity factors) closely agree with expectations for the stoichiometric composition of  $N_{\text{BMP}}:N_{\text{TFSI}}:C_{\text{TFSI}}:F_{\text{TFSI}}:S_{\text{TFSI}}:O_{\text{TFSI}}:C_{\text{BMP/hetero}}:C_{\text{BMP/alkyl}}$  of 1:1:2:6:2:4:4:5, indicative of intact molecular adsorption.

**Trends in the N 1s spectra upon Li deposition:** Next, we focus on the changes in the spectra of the adsorbed IL film introduced by stepwise post-deposition of Li (sample at r.t.), which leads to distinct modifications. These are most pronounced in the N 1s region (see Figure 1 and 3). Furthermore, the N 1s region includes information about both the cation and the anion of the IL. Hence, we will start with these spectra. For the peak fitting we kept the distance between IL-related peaks constant for all Li exposures. New peaks were added if needed to get a satisfactory fit, and held at an almost constant BE (we allowed a  $\Delta E$  of  $\sim \pm 0.2$  eV). At low amounts of Li deposited onto the sample (0.4 and 0.7 monolayer equivalents, or MLE), both the N 1s peak at around 400 eV ( $N_{\text{TFSI}}$ , blue peak in Figure 1) and at 403.3 eV ( $N_{\text{BMP}}$ , red peak in Figure 1) shift to slightly higher BEs, by about 0.2 eV. Possible reasons for this will be discussed later, together with the BEs of the other peaks. Moreover, at 0.4 MLE Li the TFSI-related peak displays an asymmetric peak shape which results from the emergence of a small additional N 1s feature (violet peak in Figure 1) at a BE of around 399.0 eV. With increasing amount of Li (0.7 MLE) this feature becomes more prominent. Furthermore, the TFSI-related N 1s feature develops an additional low-intensity peak at a BE of around 399.9 eV (green peak in Figure 1), whose nature and identification will be addressed with the spectrum for 1.4 MLE Li. The increase in intensity in the violet peak and

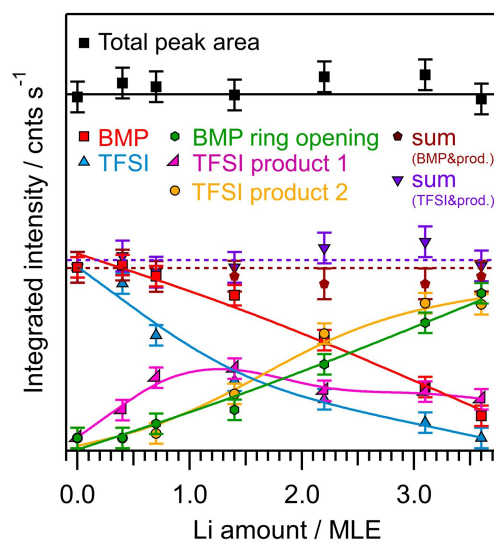


**Figure 3.** Quantitative analysis of the integrated peak intensities in the N 1s core level region vs. Li coverage.

the appearance of the green peak at 0.7 MLE go along with a loss of intensity by about 1/3 in the  $N_{\text{TFSI}}$  peak at 400.2 eV, while the intensity of the BMP-related feature does not vary significantly (less than 5%). Based on these intensity variations, we assume that the new violet peak at  $\sim 399.0$  eV results from the reaction of Li with the TFSI species of the IL, leading to a decomposition of the anion ( $N_{\text{TFSI,dec-1}}$ ).

After the next Li deposition step, to 1.4 MLE in total, we observed a small intensity decrease in the BMP-related N 1s peak at 403.5 eV (red) and a strong decrease in the TFSI-related peak (blue), which drops to about 1/3 of its initial intensity.

Furthermore, peak fitting requires an additional peak at 398.2 eV (yellow peak in Figure 1), which will also grow at higher Li doses. Since the TFSI-decomposition product reflected by the violet peak at about 399 eV does not completely compensate the loss in the  $N_{\text{TFSI}}$  peak intensity, we assume that the new peak at 398.2 eV (yellow) represents an additional decomposition product of the TFSI anion ( $N_{\text{TFSI,dec-2}}$ ). The small contribution (green), which at 0.7 MLE Li appeared at  $\sim 399.9$  eV, gets more prominent and shifts to a BE of about 400.1 eV at 1.4 MLE. This peak is identified as a separate species, different from the TFSI-related peak at 400.0 eV, based on the assumption that the total intensity of the TFSI-related peak plus peaks related to TFSI decomposition products cannot grow, but remains at best constant. Assuming the same also for the BMP-related peak intensity and its decomposition products, the green peak can be identified as being due to a BMP decomposition product ( $N_{\text{BMP,dec-1}}$ ). We also want to note that even though the blue and the green peaks have only slightly different BEs, we favor to assign them to different species, since it would be very unlikely that the original TFSI species (blue) decays upon increased Li deposition and then increases again.

At 2.2 MLE Li, we again find a significant change in the N 1s spectrum. The lower BE N 1s peak (396.0–402.0 eV) became much broader and now shows two clearly separated maxima at 398.2 eV (yellow) and 400.1 eV (green), respectively, with the first one reflecting the second TFSI decomposition product ( $N_{\text{TFSI,dec-2}}$ ) and the second one related to a decomposition product of BMP ( $N_{\text{BMP,dec-1}}$ ). In between those two peaks deconvolution reveals a contribution from the TFSI decomposition product 1 ( $N_{\text{TFSI,dec-1r}}$ , violet), which slightly decreased in intensity compared to the situation at 1.4 MLE Li. Most likely, the TFSI decomposition product 2 ( $N_{\text{TFSI,dec-2r}}$ , yellow) is a result of a further decomposition of the TFSI decomposition product 1 ( $N_{\text{TFSI,dec-1r}}$ , violet).

Finally, for Li deposition of 3.1 MLE and more, we observe a further strong decrease of the BMP-related N 1s peak to about 10–15% of its initial intensity, which goes along with an increase of the two decompositions products reflected by features at 400.1 eV ( $N_{\text{BMP,dec-1r}}$ , green) and at 398.2 eV ( $N_{\text{TFSI,dec-2r}}$ , yellow). Based on the deconvolution concept, the initial TFSI-related N 1s peak (blue) seems to have vanished completely, while the TFSI decomposition product 'TFSI<sub>dec-1</sub>' (violet), which appeared in the spectra already at very low Li exposure and reached its maximum intensity at 1.4 MLE, continued to decrease. Finally, we would like to note that there is no peak in the range of 395 to 396 eV, where the N 1s BE of  $\text{Li}_3\text{N}$  would be expected (see [28] and references therein).

In the Li 1s range, metallic Li is characterized by a peak at 55.5 eV (see the inserted spectrum). During stepwise post-deposition of Li to the pre-adsorbed IL multilayer, a peak around 56.3 eV, i.e., at higher BE compared to metallic Li, emerges and its integrated intensity gradually increases. Hence, we assume that largely  $\text{Li}^+$ -containing decomposition products contribute to this peak.

The evolution of the different N 1s components with increasing Li deposition is illustrated in Figure 3. First of all, this figure indicates that there is no loss in the total N 1s intensity,

neither for the intensity of the BMP-related peak and its decomposition product (ring opening product,  $N_{\text{BMP,dec-1}}$ ) nor for the TFSI-related peak and the decomposition products 'TFSI<sub>dec-1</sub>' and 'TFSI<sub>dec-2</sub>', which supports also our assignment. Consequently, there is no specific formation and desorption of N-containing gaseous products upon Li deposition, that could modify the elemental composition of the film. Note that molecular desorption of BMP-TFSI species, e.g., X-ray induced desorption (see Ref. [15]), cannot be excluded for a thick film. Here we also note that due to addition of Li, damping effects due to a Li cover should lead to a loss of measured N 1s intensity, which is not observed experimentally, at least not to a measurable extent. Apparently, the loss in measured N 1s intensity due to Li deposition is compensated by preferential formation of Li- and N-containing fragments in the surface near region, with the result of an essentially constant total intensity. The BMP-related peak (red) shows a more or less linear decrease in intensity with increasing Li exposure (approx. 50% loss at 2.5 MLE Li), and correspondingly, the signal of the decomposition product 'BMP<sub>dec-1</sub>' (green) increases linearly as well. This is different for the TFSI anion, where the decomposition occurs significantly faster, leading to a loss of the TFSI-related peak intensity of about 50% already between 0.7 and 1.4 MLE Li. Furthermore, there are two decomposition products 'TFSI<sub>dec-1</sub>' and 'TFSI<sub>dec-2</sub>', where the first one increases rapidly and saturates at about 1.4 MLE Li, while for the second one the increase is slower, but continues almost linearly up to the highest Li deposit dose. In the end, this latter component accounts for about 70–80% of the initial TFSI intensity.

**Reactive decomposition in multilayer vs. monolayer IL films (N 1s range):** This reaction behavior is largely, but not completely similar to the situation of Li deposition on a BMP-TFSI monolayer on HOPG.<sup>[15]</sup> In that case both the BMP and TFSI peaks seemed to decrease slightly already after the first Li dose. For larger Li deposits ( $> 0.5$  MLE), mainly the TFSI-related peak decreased, while intensity losses in the BMP-related peak were only moderate. Furthermore, only a single decomposition product with a N 1s peak at 398.9 eV appeared in the monolayer experiment, whose intensity was sufficient to fully compensate the intensity loss of the TFSI-related N 1s intensity, indicating partial transformation of TFSI into a single decomposition product. We had tentatively attributed this peak to  $\text{Li}_3\text{N}$  formation,<sup>[15]</sup> following suggestions of other decomposition studies of LiTFSI based or related electrolytes<sup>[29,30]</sup> and due to the fact that  $\text{Li}_3\text{N}$  represents a thermodynamically stable compound. Yet, comparing the N 1s BE of the decomposition product (398.9 eV) to values reported for the N 1s BE of  $\text{Li}_3\text{N}$  (395–396 eV),<sup>[28]</sup> there is a significant deviation of about 3–4 eV, which causes us to re-assign this peak to an (so far unspecified) TFSI-decomposition product. Furthermore, in contrast to the monolayer experiment, the present multilayer experiment reveals the formation of two TFSI decomposition products 'TFSI<sub>dec-1</sub>' (violet, 399.0 eV) and 'TFSI<sub>dec-2</sub>' (yellow, 398.2 eV). Another difference is that in the monolayer experiment BMP decomposition was considered to be negligible or even absent, in contrast to the decomposition in the present multilayer experiment, where a decrease of the  $N_{\text{BMP}}$  signal goes along

with the formation of a new peak ( $N_{\text{BMP,dec-1}}$ ) at 400.1 eV (green). We cannot exclude, however, that also in the monolayer experiment a BMP-related decomposition product is formed with an N 1s BE close to that of the TFSI-related N 1s peak. This would affect also our previous conclusion that desorption of N-containing species is limited to BMP or BMP-related decomposition products, while adsorbed TFSI and TFSI-related decomposition products remain on the surface.<sup>[15]</sup> On the other hand, a stabilization of BMP in interaction with the HOPG surface (no decomposition of BMP in contact with HOPG) would be consistent with results of our previous combined STM and DFT study, where we had demonstrated that the alkyl chain and the 5-membered ring of BMP are lying flat on the HOPG substrate.<sup>[13]</sup> Furthermore, additional DFT calculations revealed that in the BMP-TFSI monolayer case the underlying HOPG substrate plays an active role in the interaction with  $\text{Li}^0$  insofar as it accepts electron charge from the vapor deposited  $\text{Li}^0$ , which in turn is donated to the LUMO of TFSI, resulting in an elongation of the S–N bond and finally breaking of this bond.<sup>[15]</sup> Also this would support preferential decomposition of adsorbed TFSI upon  $\text{Li}^0$  deposition in the monolayer system, as we had proposed previously.<sup>[15]</sup> Overall, the pattern of Li induced BMP decomposition appears to differ somewhat for the monolayer film and the multilayer film.

**Trends in other spectral ranges upon Li deposition:** Next we concentrate on the changes in the F 1s, O 1s, C 1s and S 2p spectra after post-deposition of 1.4, 2.2 and 3.6 MLE of Li, respectively (Figure 2). The intensity decay of the BMP- and TFSI-related peaks upon increasing deposition of Li is summarized in Table S1 in the Supporting Information, including also the N 1s peaks. First of all, for all elements the integrated peak intensities of the TFSI-related peaks (blue) decrease and new peaks (yellow) arise, pointing to the occurrence of decomposition and desorption processes. Second, in contrast to the slight up-shift of the TFSI- and BMP-related N 1s peaks upon initial Li deposition we find no similar up-shift in the TFSI-related peaks of the other elements, which would indicate that the shifts observed in the N 1s peak are due to chemical interactions between Li and N. One should keep in mind, however, that the spectra in Figure 2 are more complex and slight shifts of the BMP-TFSI related peaks could be within the error range of the deconvolution procedure and thus cannot be fully ruled out. In the F 1s range, the gradual decrease of the  $F_{\text{TFSI}}$  peak intensity (blue) is accompanied by the appearance and growth of a new peak at lower BEs, at about 685.9 eV ( $F_{\text{TFSI,dec-1}}$ , yellow). Based on the F 1s BE, this new peak could be due to  $\text{LiF}$ , which was reported to be in the range  $685.0 \pm 0.2$  eV<sup>[31]</sup> After the last Li exposure (3.6 MLE), the total peak area had decreased to about 60% of its initial value, which points at significant desorption of F-containing but N-free (constant N 1s peak intensity) decomposition products. Most of the total F 1s intensity remained in the initial  $F_{\text{TFSI}}$  peak (44%), about 16% were transformed into the new  $F_{\text{TFSI,dec-1}}$  peak, leading to a composition of 73%  $F_{\text{TFSI}}$  and 27%  $F_{\text{TFSI,dec-1}}$  for the resulting adlayer. The remaining 40% were converted into volatile, desorbing products. Note that the result of 44% intensity of the initial  $F_{\text{TFSI}}$  peak is an upper limit, since the slight increase in

peak width of this signal, from 2.1 to about 2.3 eV, points to the formation of a decomposition product with an F 1s BE close to that of the  $F_{\text{TFSI}}$  species, which could reduce the contribution of the  $F_{\text{TFSI}}$  component.

In the O 1s range, stepwise Li deposition (1.4, 2.2 and 3.6 MLE) leads to a broadening of the TFSI-related peak, pointing to the formation of a new peak at slightly lower energy, at  $\sim 532.0$  eV ( $O_{\text{TFSI,dec-1}}$ , yellow). According to the peak deconvolution, with  $O_{\text{TFSI}}$  constrained at constant BE, the integrated intensity of the  $O_{\text{TFSI}}$  peak (blue) decreased by around 40% after the first Li dose and remained about constant after further Li deposition. In addition, after post-deposition of 3.6 MLE of Li in total, another new, low-intensity peak appeared at 529.5 eV ( $O_{\text{TFSI,dec-2}}$ , yellow). The considerable down-shift in BE points to the formation of oxide like species such as  $\text{Li}_2\text{O}$ , which was previously assigned to a signal with a BE of 528.6 eV.<sup>[32]</sup> Another study reported a peak at 530.5 eV, which developed upon exposure of a Li film to  $\text{O}_2$  at 25 K.<sup>[33]</sup> The considerable difference in BEs between these two peaks must be due to differences in the exact nature of the oxides, arising from the specific experimental conditions. Similar to our findings for the N 1s region, the total O 1s peak area remained almost constant during Li deposition, indicating that desorption of oxygen-containing species is negligible, and about 40% of the initial  $O_{\text{TFSI}}$  peak intensity were transformed into the new O-containing decomposition products  $O_{\text{TFSI,dec-1}}$  and  $O_{\text{TFSI,dec-2}}$  (remaining intensity in the  $O_{\text{TFSI}}$  component 60%, see Table S1).

The C 1s range exhibits, in addition to the peaks related to BMP-TFSI ( $C_{\text{TFSI}}$ ,  $C_{\text{BMP/hetero}}$  and  $C_{\text{BMP/alkyl}}$ , see Table 1), a low-intensity peak at the low BE side at 284.6 eV (grey), where the latter is due to the underlying HOPG substrate. Upon Li deposition, the  $C_{\text{TFSI}}$  peak gradually decreases in intensity, e.g., to 48% after the first dose, to 36% in total after the second dose and to 31% in total after the last Li dose. This is of comparable magnitude as the loss in  $F_{\text{TFSI}}$  intensity (remaining intensity 44%) upon Li deposition, considering that this value was only an upper limit (see above), which supports the assignment of these peaks to the  $\text{CF}_3$  groups. The peaks assigned to  $C_{\text{BMP/hetero}}$  and  $C_{\text{BMP/alkyl}}$  both showed a subtle up-shift of the BE after post-deposition of 1.4 MLE of Li, but no substantial changes in intensity. However, after deposition of 2.2 and 3.6 MLE of Li, respectively, the envelope of the signal ( $C_{\text{BMP/hetero}}$  and  $C_{\text{BMP/alkyl}}$  peaks) changed significantly, with the contribution from  $C_{\text{BMP/hetero}}$  becoming much less pronounced. Peak deconvolution reveals a decrease of  $C_{\text{BMP/hetero}}$  by  $\sim 17\%$  after the second and by  $\sim 49\%$  in total after the third Li dose relative to the initial intensity. On the other hand, the peak area of the  $C_{\text{BMP/alkyl}}$  peak slightly increased after the second and third Li dose by 8.4 and 10% in total, respectively. One possible explanation for these modifications is a change in the ratio of  $C_{\text{BMP/alkyl}}:C_{\text{BMP/hetero}}$  from 5:4 to 6:3 due to a ring opening reaction of BMP. Furthermore, the C 1s peak area decreased by about 11, 14 and 25% in total after the 1st, 2nd and 3rd Li dose, respectively, mainly due to the significant decrease of the intensity of the  $\text{CF}_3$  groups of TFSI. This must be related to the evolution of gaseous products, such as small fluorinated hydrocarbons. Part of the  $\text{CF}_3$  groups also decomposed into

adsorbed species, as F-containing products appeared in the F 1s regime, e.g., as LiF (see above). It is not possible, however, to identify further C-containing decomposition products in the relatively broad feature between 284–290 eV so far. Possible products falling into this category will be discussed below. Finally, comparable to the exclusion of Li<sub>3</sub>N (BE (N 1s): 395.3<sup>[28]</sup>), the formation of LiC (BE (C 1s) < 284 eV<sup>[29]</sup>) seems to be unlikely based on these spectra.

Finally, going to the S 2p range (Figure 2, right panel), stepwise Li deposition leads to a broadening of the TFSI-related peak, which can be explained by the formation of a new species at a BE of ~167.8 eV ( $S_{\text{TFSI,dec-1}}$  (S 2p<sub>3/2</sub>), yellow), which may be due to an oxy-sulphur (S–O) species (reported value 167.4 eV).<sup>[34]</sup> The integrated intensity of the  $S_{\text{TFSI}}$  peak (blue) decreased to around 53% after the first, 37% after the second and to 24% after the last Li dose. In addition, after post-deposition of 3.6 MLE of Li in total, another new, low-intensity peak emerged at 161.6 eV ( $S_{\text{TFSI,dec-2}}$ , yellow), which may be assigned to the formation of Li<sub>2</sub>S<sub>x</sub> or Li<sub>2</sub>S species, whose BEs (S 2p<sub>3/2</sub>) were reported to be around 161.5–162.9 (Li<sub>2</sub>S<sub>x</sub>),<sup>[35]</sup> 160.5 eV (Li<sub>2</sub>S)<sup>[35]</sup>, 162.1 (Li<sub>2</sub>S<sub>2</sub>)<sup>[35]</sup> and 160.7 eV (Li<sub>2</sub>S),<sup>[34]</sup> respectively. The total S 2p peak intensity decreased to 89, 86 and 84% after the 1st, 2nd and 3rd Li dose (see Table S1), respectively, indicating desorption of S-containing species. Hence, the decrease of the intensity of the  $S_{\text{TFSI}}$  peak to ~24% of the initial intensity after Li deposition (3.6 MLE) is mainly due to the transformation of the –SO<sub>2</sub> groups of TFSI into two new S-containing decomposition products (~60%), while the remaining 16% were desorbed as volatile decomposition products.

The different trends in the elemental peaks indicate that the loss in intensity of the initial TFSI-related peak differs between about 100% (N 1s) and 40% (O 1s) (see description in the text above and Table S1). Although in some cases, in particular for the  $N_{\text{TFSI}}$  peak, the peak deconvolution may allow considerable deviations from these values, it is clear, that the losses in the initial TFSI-related peaks are not identical for all elements tested. Considering the very significant losses in the measured C, F, S intensities, these cannot be explained alone by damping effects, even when considering contributions from the preferential formation of Li- and N-containing fragments in the surface near regions. Instead, this can only be explained by the partial formation of decomposition products with BEs that are very similar to that of the initial TFSI-related peak. This latter process must be least pronounced for the N 1s and the S 2p peaks, and most effective for the O 1s peak.

The situation is different when looking at the loss of total intensity for the different peaks. As illustrated in Figure 3, there is no loss of N-containing species upon reaction with Li. The same result was also obtained for oxygen and only a moderate loss of 16% is observed for sulphur (see Table S1). Hence, species containing these elements hardly desorb from the surface upon Li deposition. Instead, they are involved in spontaneous decomposition processes, leading to new surface compounds / decomposition products. This is different for the fluorine and carbon species of the CF<sub>3</sub> group of TFSI and the carbon species in the (–C–N–) group of BMP, which remain

only partly in adsorbed decomposition products, while the other part transforms into gaseous products (C<sub>x</sub>H<sub>y</sub>F<sub>z</sub>). To some extent, similar desorption processes are also active for S-containing species.

Overall, this qualitative discussion shows that the interaction of Li with BMP-TFSI multilayer films leads to the decomposition of the IL and the formation of several binary compounds such as LiF, Li<sub>2</sub>O and possibly Li<sub>2</sub>O<sub>2</sub>, and Li<sub>2</sub>S / Li<sub>2</sub>S<sub>x</sub> / Li<sub>2</sub>S<sub>2</sub> already at room temperature, together with additional more complex reaction intermediates which cannot be identified easily from these spectra.

**Reactive decomposition in multilayer vs. monolayer IL films (other spectral ranges):** Also for these peaks we can briefly compare with trends observed for the interaction of Li with a monolayer film of BMP-TFSI. First of all, in that case all IL-related peaks (F 1s, O 1s, N 1s, C 1s and S 2p) revealed a significant BE up-shift upon Li deposition, by about 1.4 eV after the first dose (ca. 1.0 MLE), while for the multilayer IL film there was hardly any change, except for small shifts for the N 1s peaks by about 0.2 eV which we had assigned to chemical interactions between Li and N before. We had previously explained the pronounced Li-induced up-shift of the IL-related peaks in the monolayer case to a vacuum level pinning effect, caused by a pronounced decrease of the work function upon Li deposition.<sup>[15]</sup> In that case, the deposited Li<sup>0</sup> donates significant charge to the topmost graphene layer, resulting in a modification of the dipole layer and thus a decrease of the work function. We tentatively explain the absence of such effects in the present case, for Li deposition on a multilayer IL film, by the lack of Li<sup>δ+</sup> ion formation at the surface and graphene surface charging, assuming that Li does not reach the interface between the IL film and HOPG, but reacts already with the IL in the initial stages of the Li deposition and diffusion process. We furthermore assume that the reaction of Li with the IL in the thick film does not lead to a significant change in work function, and thus does not induce significant changes of the BEs of the BMP-TFSI related peaks, since the reaction leads to a highly disordered product with no preferential orientation of the dipoles.

Focusing on the decomposition pathway, the mono- and multilayer experiments reveal a rather similar decomposition pattern of the TFSI anion upon contact with post-deposited Li, which is in agreement with the rather similar intensity decrease of the  $N_{\text{TFSI}}$  signal upon Li deposition in both cases. The TFSI decomposition products observed in the monolayer case had been tentatively assigned to LiF, LiOH, Li<sub>2</sub>O, Li<sub>x</sub>SO<sub>y</sub>, and Li<sub>2</sub>S,<sup>[15]</sup> most or all of which are also possible candidates for the Li-induced multilayer decomposition products of TFSI. However, in contrast to the monolayer IL case, where only a single  $N_{\text{TFSI}}$  decomposition product was observed, we now find two different products (see Figure 1 and related text). Hence, TFSI decomposition in the multilayer seems to be more complex. Furthermore, the C 1s spectra showed mainly an intensity decrease of the  $C_{\text{TFSI}}$  peak in the monolayer experiment, while the cation related  $C_{\text{BMP/hetero}}$  and  $C_{\text{BMP/alkyl}}$  peaks changed much less. Here we would like to note that the latter peak is located close to the dominating  $C_{\text{HOPG}}$  substrate peak and thus, a

quantitative analysis is problematic. Considering also the small intensity losses of the  $N_{\text{BMP}}$  peak in the monolayer experiment, this indicates that the IL monolayer film is stabilized by interaction with the underlying HOPG substrate, while it can easily react with Li in the multilayer film. In total, these experimental data provide information on the nature of the desorbing species and of simple inorganic decomposition products generated upon Li deposition onto a BMP-TFSI multilayer film at RT, but cannot unambiguously clarify the more complex intermediates formed in this process.

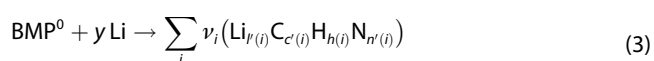
In the following we will look at the thermodynamics and kinetics of the reaction of BMP-TFSI and Li by means of DFT calculations to identify chemically reasonable candidates for possible (intermediate) products, and by comparing their calculated BEs to the experimental results we will assess whether these products might indeed be formed in the experiment.

### Thermodynamic stability of possible reaction products of BMP-TFSI and $\text{Li}^0$

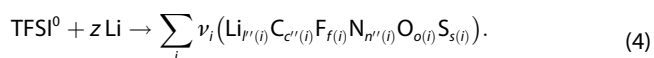
In order to determine possible products of Eq. (1) we separately studied the reaction of BMP and Li on the one hand and the reaction of TFSI and Li on the other hand. In the determination of the respective reaction energies the entropic contributions to the free energies have been neglected. Furthermore, and more severely, we assumed charge neutral products for both reactions. This implies an electron transfer from the anion  $\text{TFSI}^-$  or its products to the cation  $\text{BMP}^+$  or its products:



Under that condition Eq. (1) can be disentangled into



and

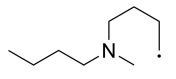
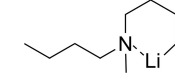
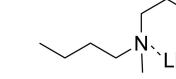
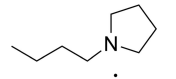
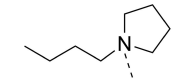
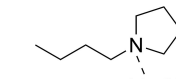
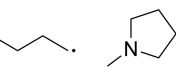
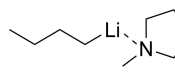
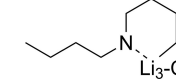


By considering the reactions of BMP and TFSI separately, mixed products of reactions involving both BMP and TFSI have been neglected. Though such products might exist, this constraint of the vast set of products might be rationalized by the fact that i) after the first Li doses mainly the N 1s peak of TFSI declines (see Figure 1 and 3), whilst the N 1s peak of BMP remains constant, and that ii) reaction between Li and  $\text{TFSI}^-$  is much more favorable than between Li and  $\text{BMP}^+$ . As far as the reduction of the cation is concerned, both one-electron and two-electron reduction mechanisms involving the formation of radical<sup>[36]</sup> or carbanion intermediates,<sup>[37]</sup> respectively, have been discussed in the literature for quaternary ammonium ions. Our RPBE–D3 gas phase calculations indicate that the one-electron reduction of  $\text{BMP}^+$  leads to a ring opening of the pyrrolidinium

ring (see Table 2, first column). In the resulting dibutylmethylamine radical the unpaired electron is located at the terminal  $\text{CH}_2$  group of one of the butyl groups. The ring opening reaction is about 0.2 eV more favorable than the elimination of a butyl- or methyl radical. This differs from the results of semiempirical quantum chemistry calculations of Kroon et al.,<sup>[38]</sup> who found the formation of methylpyrrolidin and a butyl radical to be the most likely reduction reaction of  $\text{BMP}^+$ . Random sampling of different possible conformations of the butyl group accommodating the unpaired electron of the dibutylmethylamine radical reveals that the gauche conformation and the antiperiplanar conformation are almost isoenergetic, with the gauche conformation being about 10 meV more stable. Hence, conformational differences cannot explain the deviations from the previous calculational study.<sup>[38]</sup> Instead, we tentatively ascribe the different results to the different levels of theory, semiempirical PM3<sup>[38]</sup> versus DFT calculations, that have been employed.

The radicals obtained by the one-electron reduction of  $\text{BMP}^+$  can be further stabilized by subsequent combination with neighboring radicals or Li atoms. We mainly considered reactions with Li atoms (see Table 2, second/third column). Reaction with one Li atom yields alkylpyrrolidin compounds that are energetically comparable or even more favorable than 4-(N-Butyl-N-methylamino)butyllithium, if the resulting alkyl-lithium compound is coordinated to the N atom of the pyrrolidin compound. Moreover, the calculations in the gas phase indicate that further reduction of the tertiary amine or pyrrolidin compound with in total three Li atoms to a lithium dialkylamide compound (Table 2, third column, last row) cannot be excluded, as it yields an additional energy gain of  $-3.28$  eV, which is comparable to about twice the cohesive energy of bulk Li ( $E_{\text{coh}}^{\text{RPBE}}(\text{Li}) = -1.54$  eV,  $E_{\text{coh}}^{\text{RPBE-D3}}(\text{Li}) = -1.71$  eV) and which thus corresponds to the cost of providing these Li atoms from the thermodynamically stable bulk Li metal phase. The results of these gas phase calculations are qualitatively comparable to the results obtained by calculations of reaction products of BMP and Li within the crystalline environment of BMP-TFSI.<sup>[18]</sup> The cleavage of further N–C bonds of the

**Table 2.** Energies (in eV) of possible one electron reduction products of  $\text{BMP}^+$  (first column) and subsequent reactions with one/three Li atoms (second/third column), given with respect to the 4-(N-Butyl-N-methylamino)butyl radical and isolated Li atoms.

$\text{BMP}^+ + e^-$	$\text{BMP}^+ + e^- + \text{Li}^0$	$\text{BMP}^+ + e^- + 3 \text{Li}^0$
 0.00 eV	 -2.24 eV	 -4.57 eV
 0.22 eV	 -2.59 eV	 -4.22 eV
 0.17 eV	 -2.32 eV	 -5.87 eV



dialkylamide by additional Li atoms seems to be less likely. For instance, a structure in which a methyl radical, a butylamino radical and a butyldiradical are bound to a  $\text{Li}_5$  cluster (not shown) only leads to an additional energy gain of  $-2.98$  eV with respect to the  $\text{Li}_3$ -dialkylamide compound discussed before. Thus, the absolute amount of the energy gain for the formation of this structure is less than the absolute amount of the energy gain for Li particle formation ( $2 E_{\text{coh}} = -3.08$  eV).

For comparison, we also considered the products of a Hofmann  $\beta$ -elimination following the two-electron reduction of  $\text{BMP}^+$  as suggested by Markevich et al.<sup>[6]</sup> The most favorable reactions with relative energies of  $-2.60$  to  $-2.79$  eV (see Table 3) lead to the formation of numerous, mainly volatile products which were identified as reaction products in experimental studies of metallic lithium, or galvanic couples of Li and Cu or Ni, immersed into liquid BMP-TFSI by employing gas chromatography/mass spectrometry.<sup>[39,40]</sup> These previous studies reported tertiary amines as main decomposition products such as *N*-butyl-*N*-methyl-*N*-but-3-eneamine or *N,N*-dibutyl-*N*-methylamine, methyl- and butylpyrrolidin, and (un)saturated hydrocarbons such as butane and butene. Yet, with the experimental procedure used in this work, in which Li is post-deposited on BMP-TFSI multilayers on HOPG, the one-electron reduction mechanism via radical intermediates appears more plausible. Furthermore, besides volatile products, tertiary amine or amide radicals coordinated to Li atoms or small Li clusters might persist.

Next, we concentrate on the reaction of TFSI<sup>0</sup> and atomic Li (Eq. 4). Possible reaction products were modelled in their respective crystalline bulk structures as described in the section Computation. The energies of the various reactions, which lead

to a extensive set of different decomposition products, were compared employing a grand canonical concept in which lithium is present as a reservoir. Thus, lithium enters the expression of the reaction energy  $\Delta E$  (Eq. 5) by means of its chemical potential ( $\mu_{\text{Li}}$ ). To obtain the reaction energy for the whole reaction of BMP-TFSI and Li, we included the cohesive energy of BMP-TFSI via Eq. 2 and the energy of the reaction of  $\text{BMP}^0$  and Li via Eq. 3. For the latter reaction we only considered the initial reaction of  $\text{BMP}^0$  and one Li atom to 4-(*N*-Butyl-*N*-methylamino)butyllithium.

$$\Delta E = \sum_i \nu_i E(\text{product}_i) - E(\text{BMP} - \text{TFSI}) - x\mu_{\text{Li}} \quad (5)$$

where  $\nu_i$  denotes the stoichiometric factor and  $E(\text{product}_i)$  the energy per formula unit of the *i*-th product of the reaction of TFSI<sup>0</sup> or  $\text{BMP}^0$  and Li.  $E(\text{BMP} - \text{TFSI})$  is the energy per formula unit of the BMP-TFSI crystal and  $x$  is the number of Li atoms involved in the reaction. Furthermore, the chemical potential of Li can be split into the chemical potential of bulk Li at zero temperature and pressure, i. e., the energy of bulk Li ( $E(\text{Li})$ ), and a remaining part ( $\Delta\mu_{\text{Li}}$ ) depending on temperature and pressure (or concentration):  $\mu_{\text{Li}} = E(\text{Li}) + \Delta\mu_{\text{Li}}$ . Although it is likely that in the UHV experiments thermodynamic equilibrium conditions are not reached, the Li chemical potential can be used in the calculations as a control parameter to identify the most likely products upon Li deposition. For comparison with realistic battery situations it is also important to note that the difference in the Li chemical potentials in anode and cathode controls the open circuit potential of Li-ion batteries.<sup>[41]</sup>

Plotting  $\Delta E$  against  $\Delta\mu_{\text{Li}}$  we can determine the most stable reaction products, i. e., the products of the reactions with the lowest reaction energies at a given chemical potential of Li. The results are shown in Figure 4. The most stable products at different ranges of the chemical potential of Li are highlighted as solid colored lines and denoted in the legend. For large parts of the phase diagram LiCN is among the most stable products. In detail, at a low chemical potential (which at a given temperature corresponds to a low concentration) of Li there is a very narrow range (range I:  $-2.95 < \Delta\mu_{\text{Li}} < -2.94$  eV) in which the formation of LiCN,  $\text{LiSO}_2\text{F}$ ,  $\text{Li}_2\text{S}$ , LiF and  $\text{CO}_2$  is favoured. In the range of  $-2.94$  eV  $< \Delta\mu_{\text{Li}} < -2.3$  eV (range II) the most stable products are again LiCN,  $\text{LiSO}_2\text{F}$ ,  $\text{Li}_2\text{S}$ , LiF but also solid  $\text{Li}_2\text{CO}_3$  instead of gaseous  $\text{CO}_2$ . Increasing the chemical potential of Li further up to  $-1.30$  eV leads to the decomposition of  $\text{LiSO}_2\text{F}$  into  $\text{Li}_2\text{S}$ ,  $\text{Li}_2\text{O}$  and LiF (range III). In the range of  $-1.30$  eV  $< \Delta\mu_{\text{Li}} < -0.52$  eV (range IV)  $\text{Li}_2\text{CO}_3$  is decomposed into  $\text{Li}_2\text{O}$  and LiC. Only at  $\Delta\mu_{\text{Li}} > -0.52$  eV (range V) the reaction  $\text{LiCN} + 3\text{Li} \rightarrow \text{LiC} + \text{Li}_3\text{N}$  gets energetically favoured and TFSI is completely decomposed into the binary Li compounds of its elements:  $\text{Li}_3\text{N}$ , LiC,  $\text{Li}_2\text{S}$ ,  $\text{Li}_2\text{O}$  and LiF. The most stable products found at the chemical potential of bulk Li ( $\Delta\mu_{\text{Li}} = 0$ ) agree with ab initio molecular dynamics simulations of the interface between Li-TFSI and Li, in which complete decomposition of TFSI has been revealed.<sup>[21]</sup> Interestingly, employing a larger supercell in their calculation, those authors also found the formation of CN moieties, which remained stable during the

**Table 3.** Energies (in eV) of possible products of the two electron reduction reaction of  $\text{BMP}^+$  and subsequent Hofmann  $\beta$ -elimination of  $\text{BMP}^+$  cations given with respect to two 4-(*N*-Butyl-*N*-methylamino)butyl radicals.

	$-1.33$ eV
	$-2.52$ eV
	$-2.71$ eV
	$-1.22$ eV
	$-2.41$ eV
	$-2.61$ eV
	$-1.40$ eV
	$-2.60$ eV
	$-2.79$ eV

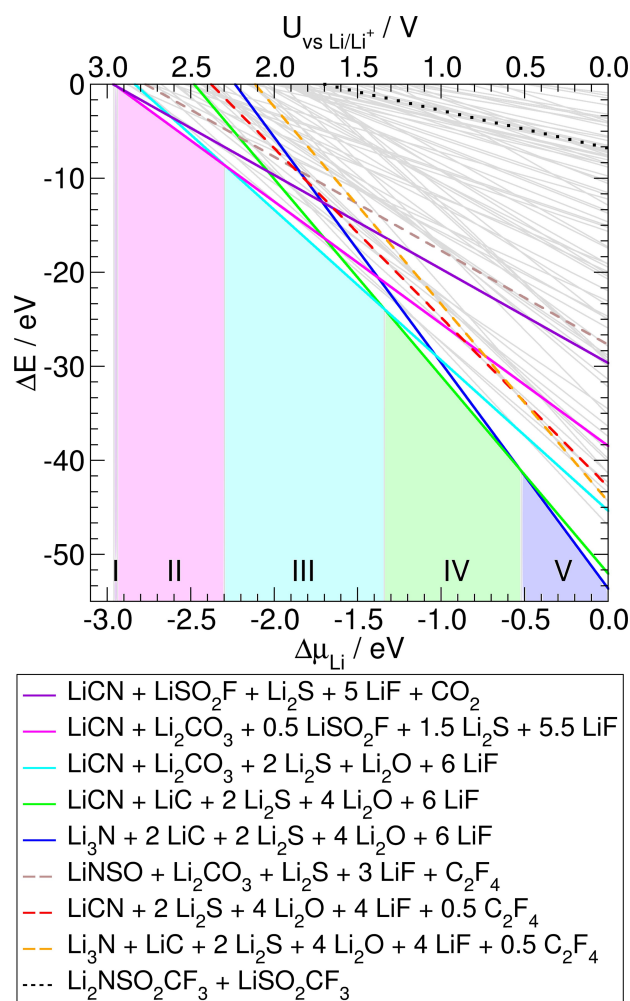


**Figure 4.** Reaction energies  $\Delta E$  as a function of the chemical potential of Li ( $\Delta\mu_{\text{Li}}$ ) or of the electrode potential ( $U$  vs  $\text{Li}/\text{Li}^+$ ) according to Eqs. 5 and 8. Colored solid lines mark the most stable products. Colored dashed lines highlight the most stable products of reactions including evolution of  $\text{C}_2\text{F}_6$  or  $\text{C}_2\text{F}_4$ . The respective products are denoted in the legend. The black dotted line denotes the reaction to  $\text{Li}_3\text{NSO}_2\text{CF}_3$  and  $\text{LiSO}_2\text{CF}_3$  as possible model for the initial reaction. The grey lines correspond to other possible product combinations that were considered.

runtime of the simulation (164 ps). They argued that the trajectory in case of the larger supercell might not be long enough to reach complete decomposition of TFSI. On the other hand, our calculations indicate that the formation of LiCN is thermodynamically more stable than the formation of  $\text{Li}_3\text{N}$  and LiC at chemical potentials lower than  $-0.52$  eV. Hence, the number of Li atoms per TFSI may be too low in the mentioned AIMD study to reach the formation of  $\text{Li}_3\text{N}$ . Next, we would like to point out that in non-equilibrium situations, as encountered when a product desorbs, the initial reduction products might be decisive for the path of the reaction and thus the nature of the final products. As shown in the section Experimental Results, our XPS experiments indicate the desorption of C- and F-containing species. Therefore, Figure 4 highlights the most stable reaction products of the subgroup of the reactions that include the evolution of  $\text{C}_2\text{F}_4$  or  $\text{C}_2\text{F}_6$  as dashed lines. At low chemical potentials (range Ib,  $-2.80$  eV  $< \Delta\mu_{\text{Li}} < -1.90$  eV)

$\text{LiNSO}$ ,  $\text{Li}_2\text{CO}_3$ ,  $\text{Li}_2\text{S}$ , LiF and  $\text{C}_2\text{F}_4$  are found as most stable reduction products. For chemical potentials in the range Ib ( $-1.90$  eV  $< \Delta\mu_{\text{Li}} < -0.52$  eV) we find the decomposition of TFSI to LiCN,  $\text{Li}_2\text{S}$ ,  $\text{Li}_2\text{O}$ , LiF and  $\text{C}_2\text{F}_4$ . LiCN will then, as already mentioned above, decompose to LiC and  $\text{Li}_3\text{N}$  above a chemical potential of Li of  $-0.52$  eV.

Further comparison to experiments is difficult, as thermodynamic equilibrium might not always be reached. Still, the thermodynamically stable structures at different Li conditions could serve as starting point for comparison. In case of UHV experiments, e.g., as described in the section Experimental Results, only a narrow range of  $\Delta\mu_{\text{Li}}$  is probed: by changing the amount of Li by a factor of 10,  $\Delta\mu_{\text{Li}}$  only changes by about  $k_B T \ln(10) = 0.059$  eV at room temperature. Furthermore, it is rather difficult to assign UHV experiments to a specific  $\Delta\mu_{\text{Li}}$ . Very roughly the maximum number of Li-atoms per ion pair can be estimated based on three assumptions: first, a homogeneous distribution of post-deposited Li atoms is assumed and the atomic density of 1 MLE of Li corresponds to the atomic density within the (110) plane of the bcc Li crystal ( $0.11$  Li atoms/ $\text{\AA}^2$ ), second, the surface of the BMP-TFSI multilayer corresponds to the (100) plane of the BMP-TFSI crystal and third, all Li atoms react with surface TFSI ions. This yields a ratio of at most 6 Li atoms per 1 TFSI ion for 1 MLE of Li, i.e., the maximum experimentally employed dose of 3.6 MLE Li corresponds to 22 Li atoms per TFSI ion. Stoichiometrically, 23 Li atoms per TFSI are needed for the complete decomposition of TFSI to the binary compounds  $\text{Li}_3\text{N}$ ,  $\text{Li}_2\text{S}$ ,  $\text{Li}_2\text{O}$ , LiC and LiF. The respective reaction of TFSI to LiCN requires only 20 Li atoms per TFSI. Thus, presumably, the UHV experiments are performed in a range of the chemical potential of Li, where the reaction to LiCN is possible, while the amount of Li atoms seems to be too low for the (complete) reaction to  $\text{Li}_3\text{N}$ .

These calculations may also be used for the prediction of reaction products in an electrochemical system. In the presence of an electrode potential  $U$  the chemical potential needs to be replaced by the electrochemical potential (Eq. 6)

$$\tilde{\mu} = \mu + neU \quad (6)$$

where  $n$  denotes the charge of the particle. Analogously to the concept of the computational hydrogen electrode,<sup>[42]</sup> a computational Li electrode<sup>[43]</sup> can be employed in which the equilibrium (Eq. 7)



is used to define a suitable reservoir. Thus, the change in the electrochemical potential of the solvated  $\text{Li}^+$  ion is given by

$$\Delta\tilde{\mu}_{\text{Li}^+} = -eU_{\text{vs Li}/\text{Li}^+} + k_B T \ln(a_{\text{Li}^+}) \quad (8)$$

where  $U_{\text{vs Li}/\text{Li}^+}$  is the applied electrode potential versus  $\text{Li}/\text{Li}^+$ . In a first approximation the dependency of the electrochemical potential on the activity may be neglected, due to the fact that, according to Eq. 8,  $\Delta\tilde{\mu}_{\text{Li}^+}$  only changes by 60 meV when changing the activity by an order of magnitude, which is a

small contribution, compared to the contribution of the electrode potential that is typically varied by several Volts vs Li/Li<sup>+</sup>. Hence, the stability of various reaction products can be given as a function of the applied electrode potential (see upper axis of Figure 4). As the reduction potential of a species is determined by its initial reduction reaction, we need to look at the initial reduction products of BMP-TFSI. According to previous studies,<sup>[18,44,45]</sup> and as it will be shown in the next section, we may assume LiSO<sub>2</sub>CF<sub>3</sub> and Li<sub>2</sub>NSO<sub>2</sub>CF<sub>3</sub> as rough models for the initial reduction products of BMP-TFSI. Employing the respective bulk structures, we find their formation energetically possible at (electro)chemical potentials  $\Delta\mu_{\text{Li}} > -1.7$  eV (or  $U < 1.7$  V vs Li/Li<sup>+</sup>) (see dotted line in Figure 4). For comparison, the experimental reduction potential of LiTFSI dissolved in BMP-TFSI is reported to be in the range around 1.4 to 1.6 V vs Li/Li<sup>+</sup>.<sup>[5,7]</sup> Furthermore, calculations employing an implicit solvation model with the dielectric constant of water also report the reduction potential of TFSI<sup>-</sup> to be 1.4 V vs Li/Li<sup>+</sup>.<sup>[44]</sup> Hence, our simple model yields results comparable to both experimental and calculated reduction potentials reported in the literature.<sup>[7,44]</sup> Moreover, according to Figure 4, we expect the electrochemical reduction of TFSI to occur in a range of  $\Delta\mu_{\text{Li}}$  where LiCN, LiF, Li<sub>2</sub>S, Li<sub>2</sub>O are the most stable products, accompanied either by Li<sub>2</sub>CO<sub>3</sub> for  $\Delta\mu_{\text{Li}} < -1.3$  eV or at higher (electro)chemical potentials by the further decomposed product LiC. This also implies that only in electrochemical studies that lower the potential to less than 0.5 V vs Li/Li<sup>+</sup> Li<sub>3</sub>N can be found as thermodynamical product.

We note that neither the actual interaction with a substrate nor interphases between different products are considered in this simple comparison of reaction energies that are based on the bulk energies of crystalline structures of the products. Furthermore, entropic contributions that might favour the formation of gaseous products compared to solid products are not taken into account. Additionally, stabilizations via phase transitions such as  $2 \text{LiCN} \rightarrow \text{C} + \text{Li}_2\text{CN}_2$  have been disregarded. Finally, the impact of an explicit Li<sup>+</sup>-coordination and thus the impact of the local Li<sup>+</sup> concentration on the reduction potential has not been studied in detail. For instance, as shown by quantum chemical calculations in Ref. [44], the reduction potential of Li<sub>2</sub>TFSI<sup>+</sup> amounts to 2.3–2.9 V vs Li/Li<sup>+</sup>, whereas a value of 1.4 V vs Li/Li<sup>+</sup> is calculated for the bare TFSI<sup>-</sup> anion.

Nevertheless, looking at the products in thermodynamic equilibrium can be a first step to elucidate probable SEI components, in particular as longish AIMD simulations such as done in Ref. [21] are not applicable to a broad range of electrolytes and different Li concentrations. The stability of different sets of products at varying Li potential/concentration can give correct trends regarding the decomposition of electrolytes that interact mainly electrostatically or via van der Waals forces with the electrode.

In the next section we shortly elucidate the possibility of kinetic barriers in the course of the reaction of BMP-TFSI and Li.

### Kinetic stability of intermediate products of the reaction of TFSI<sup>-</sup> and Li<sup>0</sup>

To model the initial reaction of TFSI<sup>-</sup> and individual Li atoms, an isolated, charge neutral Li-TFSI complex, that has been optimized within a polarizable continuum model, is used as input structure. The addition of an electron to this complex within the implicit solvation model and a subsequent geometry optimization yields a structure in which the N–S bond is immediately broken. The reaction energy with respect to the TFSI<sup>-</sup> anion and one Li atom amounts to  $-1.92$  eV. Optimized structures with broken S–C or C–F bonds are only about 0.08 eV or 0.17 eV less favorable (see Figure 5a–c). In Figure 5d–f reaction products with two coordinating Li atoms are shown. Their respective reaction energies are specified as well. We note, that the reaction energies are given per Li atom. Thus, the reaction of TFSI<sup>-</sup> and Li rather leads to the formation of fragments coordinated by two Li atoms and leaving half of the TFSI<sup>-</sup> molecules unreacted, than to the fragmentation of all TFSI<sup>-</sup> molecules to structures coordinated by one Li atom each. Comparing the reaction products coordinated by two Li atoms (see Figure 5d–f), the cleavage of the C–F bond seems slightly favored. Structures involving N–S or S–C bond breaking are again only slightly about 0.06 or 0.13 V less stable. As the intermolecular stabilization of the resulting fragments due to explicit coordination to neighboring molecules is lacking within the implicit solvation model used here, the results are not rigorously comparable to the results of geometry optimizations in which the ionic liquid environment is taken into account explicitly. Nevertheless, though structurally slightly different, the reaction energies per Li atom calculated with the implicit solvent model for the reaction of TFSI<sup>-</sup> and one or two Li atom(s) to structures in which either one N–S, one S–C or one C–F bond is broken are in the same range as the corresponding reaction energies per Li atom calculated with an explicit

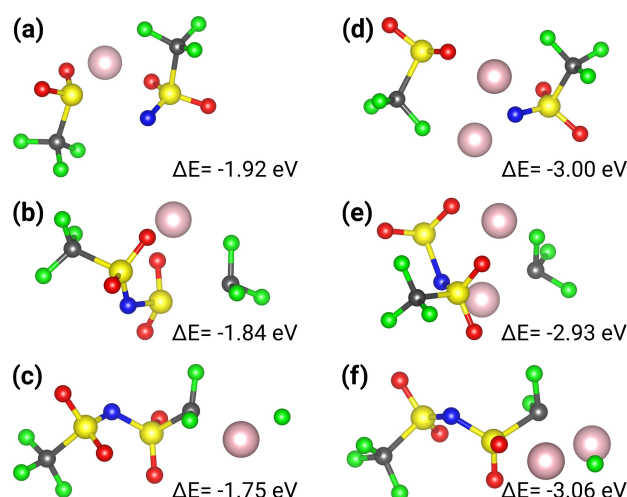
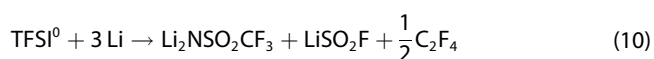
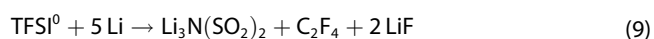


**Figure 5.** Products and energies of the reaction of TFSI<sup>-</sup> and one Li atom (a–c) or two Li atoms (d–f) involving N–S bond breaking (a, d), S–C bond breaking (b, e) or C–F bond breaking (c, f). The reaction energies  $\Delta E$  are given per Li atom and referred to the energies of an isolated TFSI<sup>-</sup> anion and an isolated Li atom calculated by employing the implicit solvation model CPCM.

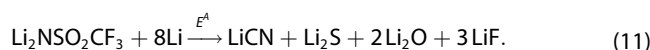
environment. Previously, we reported values of  $-1.89$ ,  $-1.87$  and  $-1.80$  eV for structures with a broken N–S, S–C or C–F bond, respectively, for the reaction of TFSI<sup>−</sup> with one Li atom.<sup>[18]</sup> For the reaction of TFSI<sup>−</sup> with two Li atoms the reaction energies per Li atom in an explicit BMP-TFSI environment amount to  $-3.00$ ,  $-2.78$  and  $-2.88$  eV for structures with a broken N–S, S–C or C–F bond, respectively.<sup>[18]</sup> For comparison, the reaction energies per Li atom calculated for the reaction of BMP<sup>+</sup> and one or two Li atoms within the implicit solvation model are  $-1.17$  or  $-1.46$  eV ( $-1.31$  eV or  $-1.55$  eV in an explicit environment<sup>[18]</sup>). Thus, this reaction is less likely than the reaction of TFSI<sup>−</sup> and Li. Consequently, in the course of the reaction of BMP-TFSI and Li atoms, the immediate formation of a NSO<sub>2</sub>CF<sub>3</sub> intermediate seems to be the most likely initial reaction. Yet, intermediates with broken S–C or C–F bonds are only slightly less stable and thus their formation might be possible as well. Taking into account that desorption of volatile C- and F-containing species has been deduced from experiment, possible initial reactions might be:



Although no reaction barrier is found for the initial reaction, subsequent reaction steps to the thermodynamical products such as LiCN, Li<sub>2</sub>CN<sub>2</sub> or Li<sub>3</sub>N, as determined in the previous section, could still be associated with reaction barriers. As shown in Figure 6, Li structures in which a N–C bond is formed, are by about 0.81 to 1.56 eV more stable than the initial LiN(SO<sub>2</sub>CF<sub>3</sub>)(SO<sub>2</sub>) or Li<sub>2</sub>NSO<sub>2</sub>CF<sub>3</sub> fragments. Besides, NEB calculations show, that there are considerable barriers of 2.81 eV (Figure 6a), 2.34 or 1.59 eV (Figure 6b) for the intramolecular rearrangement from an S–C bond to an N–C bond. On the other hand, Figure 6b shows, that the reaction barrier is about 0.75 eV smaller if the S–C bond breaking and N–C bond formation are accompanied by a C–F bond breaking and Li–F bond formation process (shown in red in Figure 6b). The

transition state of that reaction no longer relates to the S–C bond breaking but to the C–F bond breaking. Thus, at a ratio of one or two Li atom(s) per TFSI<sup>−</sup> molecule, there are substantial barriers for the formation of N–C compounds whose formation is thermodynamically clearly favored. Correspondingly, the initially formed N(SO<sub>2</sub>CF<sub>3</sub>)(SO<sub>2</sub>) or NSO<sub>2</sub>CF<sub>3</sub> fragments might persist due to kinetic barriers, in particular at low Li concentrations. Upon increasing the Li concentration the electron density at the molecular fragment will be enhanced, which destabilizes the fragment further and presumably lowers the barrier for further decomposition processes. Indeed, comparing Figure 6a with one Li atom per TFSI fragment and Figure 6b with two Li atoms per TFSI fragment already reveals a decrease in the barrier for the intramolecular rearrangement of about 1.2 eV. Employing 4 Li atoms per NSO<sub>2</sub>CF<sub>3</sub> fragment in a geometry optimization leads to an immediate decomposition of the educt and finally to a fragment with an N–C bond.

To sum up, an immediate decomposition of TFSI<sup>−</sup> due to its interaction with Li<sup>0</sup> was revealed. Yet subsequent reactions of initial products are kinetically hindered by an energy barrier  $E^{\ddagger}$ , such as,



The existence of such kinetically controlled initial products as XPS detectable intermediates will be verified by comparison to experiment in the next section.

### Calculated core level binding energies and comparison to experiment

In order to further validate the actual formation of intermediate or thermodynamic products, core level binding energies (BEs) of various possible products were computed and compared to the results of the XPS measurements (see section Experimental Results). The BEs of BMP-TFSI and the decomposition products resulting from reaction with Li were calculated along the procedure described in the section Computation. To obtain

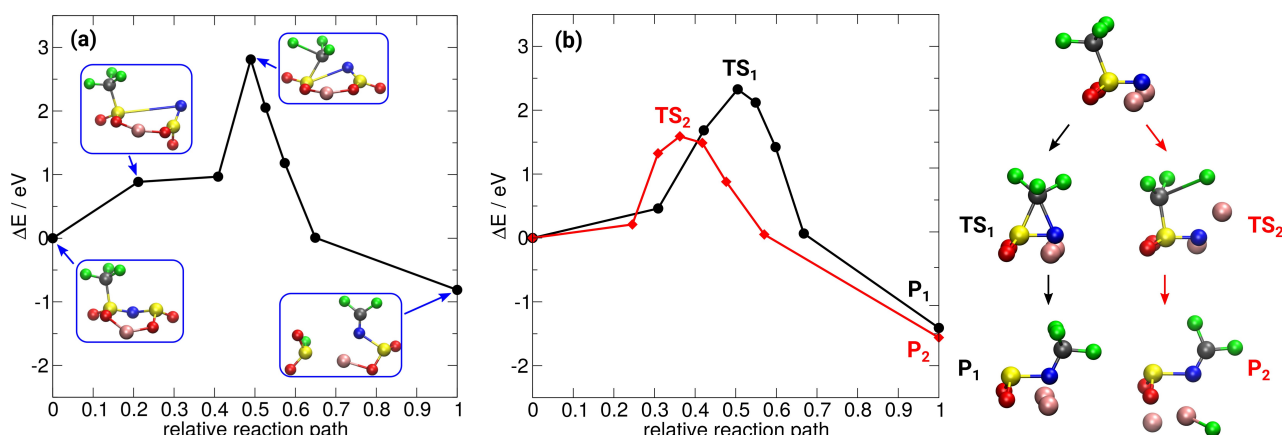


**Figure 6.** Minimum energy paths of intramolecular rearrangements of (a) LiN(SO<sub>2</sub>)(SO<sub>2</sub>CF<sub>3</sub>) or (b) Li<sub>2</sub>NSO<sub>2</sub>CF<sub>3</sub> in which the S–C bond is broken and a N–C bond is formed.

absolute values with respect to the Fermi level we calibrated the calculated results by comparison with experimental data, using the BEs of the atoms in the TFSI anion (see Table 1) as reference, and assuming the same vacuum level alignment for the larger fragments as present for BMP-TFSI (see section Computation). In contrast, the smaller, inorganic binary fragments are assumed to form close to the surface of the substrate, where a Fermi level alignment of these compounds might be more appropriate. In a first comparison of computation and experiment we calculated the N 1s BE in BMP within a BMP-TFSI crystal. The resulting value (403.7 eV, first row in Table 4) is in good agreement with the peak at 403.3 eV observed experimentally for BMP-TFSI multilayers on HOPG. Hence, using the atoms in the anion as reference, the N 1s of the cation is only by a few tenths of an eV off from the experimental value. The resulting core level BEs calculated for the various products of the reaction of Li and TFSI and of Li and BMP are summarized in Tables 4 and 5, respectively.

Next, we can compare calculated BEs with experimental values for binary inorganic compounds measured here or known from the literature such as LiF,<sup>[31]</sup> Li<sub>2</sub>O, Li<sub>2</sub>O<sub>2</sub>, Li<sub>3</sub>N<sup>[28]</sup> or Li<sub>2</sub>S.<sup>[34,35]</sup> To this end the calculated BEs and our experimental spectra are shown together in Figure 7. For LiF, the calculated F 1s BE of 684.9 eV agrees very well with the value of 685.0 eV reported previously<sup>[31]</sup> and also with the position of the TFSI decomposition peak ( $F_{\text{TFSI,dec-1}}$ , Figure 7) of 685.9 eV. Alternatively, the new peak could be assigned to the formation of LiSO<sub>2</sub>F (computed BE: 685.0 eV (Table 5)). In that case, the related O 1s peak (computed BE: 531.6 eV) would be close to the  $O_{\text{TFSI,dec-1}}$  peak at 531.6 eV, while the related S 2p peak (computed BE: 166.3 eV) would be somewhat lower than the range of the main S 2p peak, leaving this species, at least on a first view, less probable (see our later discussion of LiSO<sub>2</sub>F).

Similarly, the new O 1s peak at 529.5 eV appearing upon Li deposition ( $O_{\text{TFSI,dec-2}}$ , Figure 7) agrees well with the O 1s BE of 529.8 eV calculated for Li<sub>2</sub>O, and is well in the range of experimental values reported previously for this compound.<sup>[28,32]</sup> Based on the calculations, however, this peak may also be related to a Li<sub>2</sub>O<sub>2</sub> species (computed BE: 529.2 eV).

Focusing on the N 1s and C 1s peaks, we assume that the TFSI decomposition product represented by the  $N_{\text{TFSI,dec-2}}$  peak at 398.2 eV (Figure 7) refers to the energetically stable LiCN species, whose N 1s BE is computed to be 398.4 eV. The related C 1s peak (computed BE: 285.6 eV) would be in the broad C 1s

**Table 4.** Computed N 1s core level binding energies (in eV) for different products of the reaction of BMP (NC<sub>9</sub>H<sub>20</sub>) and Li. The N 1s core level binding energy of TFSI within the BMP-TFSI crystal has been used for calibration against experiment.

NC <sub>9</sub> H <sub>20</sub> -TFSI	403.7
·NC <sub>9</sub> H <sub>20</sub>	400.1
LiNC <sub>9</sub> H <sub>20</sub>	401.3
LiF·NC <sub>9</sub> H <sub>20</sub>	400.3
lithium butylmethylamide	399.0
N-methylpyrrolidine	402.1
N-butylpyrrolidine	402.0
N-butyl-N-methyl-N-but-3-eneamine	400.4
N,N-dibutyl-N-methylamine	400.9

**Table 5.** Computed core level binding energies in eV for different products of the reaction of TFSI and Li. Core level binding energies of TFSI within the BMP-TFSI crystal (first row) have been aligned to experiment. For comparison, the range of various experimental values are given for Li<sub>3</sub>N, Li<sub>2</sub>S<sub>2</sub>, Li<sub>2</sub>S, Li<sub>2</sub>O, Li<sub>2</sub>O<sub>2</sub>, LiC and LiF.

	N 1s	S 2p	O 1s	C 1s	F 1s
BMP-N(SO <sub>2</sub> CF <sub>3</sub> ) <sub>2</sub>	400.0	169.6	533.3	293.5	689.6
Li <sub>2</sub> N(SO <sub>2</sub> CF <sub>3</sub> )(SO <sub>2</sub> CF <sub>2</sub> )	399.7	169.3	533.2	293.1	689.2
				(CF <sub>3</sub> )	(CF <sub>3</sub> )
				289.0	688.1
				(CF <sub>2</sub> )	(CF <sub>2</sub> )
Li <sub>2</sub> N(SO <sub>2</sub> CF <sub>3</sub> )(SO <sub>2</sub> )	399.1	169.4	533.6	293.3	689.2
		(SO <sub>2</sub> CF <sub>2</sub> )	(SO <sub>2</sub> CF <sub>3</sub> )		
		167.1	532.1		
		(SO <sub>2</sub> )	(SO <sub>2</sub> )		
Li <sub>3</sub> N(SO <sub>3</sub> ) <sub>2</sub>	398.9	167.5	532.6		
Li <sub>2</sub> NSO <sub>2</sub> CF <sub>3</sub>	398.8	169.4	533.7	293.1	689.5
LiN(CF <sub>2</sub> )(SO <sub>2</sub> )	398.9	166.9	532.0	290.8	689.2
LiNSO <sub>2</sub>	400.1	170.3	533.7		
Li <sub>2</sub> NSO <sub>2</sub>	399.6	169.5	533.4		
LiNSO	395.7	163.9	530.1		
Li <sub>2</sub> CN <sub>2</sub>	398.8			287.7	
LiCN	398.4			285.6	
Li <sub>3</sub> N	394.3				
	395.2–				
	396.0 <sup>[a]</sup>				
LiSO <sub>2</sub> CF <sub>3</sub>		166.9	532.6	292.2	688.9
LiSO <sub>3</sub> CF <sub>3</sub>		170.5	534.1	293.9	689.6
LiSO <sub>2</sub> F		166.3	531.6		685.0
LiSO <sub>3</sub> F		170.1	533.7		688.0
Li <sub>2</sub> SO <sub>4</sub>		170.8	534.0		
Li <sub>2</sub> SO <sub>3</sub>		168.7	533.4		
Li <sub>2</sub> SO <sub>2</sub>		164.0	531.2		
LiSO <sub>2</sub>		164.8	531.4		
Li <sub>2</sub> SO		161.0	529.9		
Li <sub>2</sub> S <sub>2</sub>		161.1			
		162.1 <sup>[b]</sup>			
Li <sub>2</sub> S		160.8			
		160.5;			
		160.7 <sup>[b,c]</sup>			
Li <sub>2</sub> O			529.8		
			528.3–		
			531.9 <sup>[a,b]</sup>		
Li <sub>2</sub> O <sub>2</sub>			529.2		
			530.9–		
			533.1 <sup>[a]</sup>		
Li <sub>2</sub> CO <sub>3</sub>			532.9	290.3	
LiC				282.1	
				284 <sup>[e]</sup>	
LiF					684.9
					685.0 <sup>[f]</sup>

[a] Ref. [28] and ref. therein. [b] Ref. [35] [c] Ref. [34] [d] Ref. [32] [e] Ref. [29] [f] Ref. [31].

peak ranging from 284 to 289 eV, and could not be identified separately. Based on the calculated BEs, this N 1s peak could also be due to Li<sub>2</sub>CN<sub>2</sub> (computed BE: 398.8 eV), and also in this case the C 1s signal would appear in the broad C 1s peak (computed BE: 287.7 eV). The calculations also support our previous conclusion that the formation of Li<sub>3</sub>N species can be ruled out, as both the computed N 1s BE of 394.3 eV and the experimental values (BE (N 1s): 395.3<sup>[28]</sup>) are lower than the lowest BE peak at about 398 eV. The same is also true for the possible formation of LiC, as the computed C 1s BE would be outside the range of experimental signals (computed BE: 282.1 eV, experiments value < 284 eV<sup>[29]</sup>).

Finally, for the S 2p spectra, the low-intensity peak emerging at 161.6 eV after deposition of 3.6 ML Li ( $S_{\text{TFSI,dec-2}}$  Figure 7), may be assigned to the formation of  $\text{Li}_2\text{S}$  or  $\text{Li}_2\text{S}_2$  species whose BEs (S 2p<sub>3/2</sub>) were calculated to be 160.8 and 161.1 eV, respectively. This is in good agreement also with previous experimental values reported for these species (160.5 eV<sup>[35]</sup> and 160.7 eV<sup>[34]</sup> for  $\text{Li}_2\text{S}$ , 162.1 eV for  $\text{Li}_2\text{S}_2$ <sup>[35]</sup>).

We note that the apparently good agreement of calculated and experimental BEs of the binary inorganic compounds given with respect to the Fermi level is to some extent due to a fortious cancellation of errors. As shown in Table 6, the calculated BEs given with respect to the valence band maximum tend to overestimate the actual experimental values. On the other hand, GGA is well-known to underestimate the band gap of such insulating materials. Consequently, at least a partial cancellation of errors occurs, when the BEs of large band gap materials, such as  $\text{Li}_2\text{O}$  or  $\text{LiF}$ , are calculated according to Eq. 14.

In principle, one could derive further information on the presence of specific compounds by comparison of the respective peak intensities, which should obey the stoichiometric composition of the different compounds. Because of the little differences in the Li 1s BEs of the different compounds and the considerable number of possible combinations this is, however, not possible in the present case.

In a third step we finally tried to identify the different, more complex reaction intermediates of BMP-TFSI and Li. Starting with possible TFSI decomposition products we find that fragments in which one or both  $\text{CF}_3$  groups or one  $\text{SO}_2\text{CF}_3$  group are abstracted lead to N 1s BEs of 398.8 to 399.1 eV (see row 3–5 in Table 5), in very good agreement with the experimental findings for  $N_{\text{TFSI,dec-1}}$  (violet peak, Figure 1). The resulting initial fragments  $\text{Li}_2\text{N}(\text{SO}_2\text{CF}_3)(\text{SO}_2)$  and  $\text{Li}_2\text{NSO}_2\text{CF}_3$ , whose formation is almost isoenergetic (see Figure 5), and also the fragment  $\text{Li}_3\text{N}(\text{SO}_2)_2$  can explain the N 1s peak at around 399 eV (violet peak). The validity of these assignments can be tested by comparison of the experimental and calculated BEs of the other elemental peaks of these compounds, including the O 1s, C 1s, F 1s and S 2p peaks. For an overview the agreement between the BEs calculated for the different intermediates and the experimental spectra is illustrated in Figure 7. For the O 1s spectral range, the two fragments  $\text{Li}_2\text{N}(\text{SO}_2\text{CF}_3)(\text{SO}_2)$  and  $\text{Li}_2\text{NSO}_2\text{CF}_3$  show computed BEs for the  $\text{SO}_2\text{CF}_3$  group of 533.6 and 533.7 eV, which is very close to that of the TFSI anion (533.2 eV) and could not be distinguished from that, while for the  $\text{SO}_2$  groups we find substantially lower BEs (532.1 and

532.6 eV), which would fit to the new  $O_{\text{TFSI,dec-1}}$  peak at 532.0 eV. Similarly, for the S 2p peak, these two fragments show computed BEs for the  $\text{SO}_2\text{CF}_3$  group of 169.4 eV, which is also very close to that of the TFSI anion (169.6 eV) and could not be distinguished from that, while for the  $\text{SO}_2$  groups we find substantially lower BEs (167.1, 167.5 eV). The latter ones could be part of the broader new peak  $S_{\text{TFSI,dec-1}}$  (yellow peak, Figure 2) centered at 167.8 eV. Finally, the C 1s and F 1s BEs of the remaining  $\text{CF}_3$  group (293.3–293.1, 689.2–689.5 eV) would be very close to that of the TFSI anion (293.5, 689.6 eV), and could be integrated in these peaks. In total, all three fragments mentioned in row 3–5 in Table 5 would be possible reaction intermediates based on the measured and computed BEs of peaks in the different spectral ranges. Similar as for the binary compounds, a further evaluation based on the ratios of the peak intensities is not possible due to the large number of possible combinations.

Furthermore, also the subsequent abstraction of an F atom from the  $\text{Li}_2\text{N}(\text{SO}_2)(\text{CF}_3)$  intermediate, followed by an intramolecular rearrangement of the resulting  $\text{CF}_2$  group, results in a compound ( $\text{LiN}(\text{CF}_2)(\text{SO}_2)$ ) with an N 1s BE of 398.9 eV. In this case, the computed BEs of the O1s and S 2p signals (166.9, 532.0 eV) would be in the same range as obtained for the  $\text{SO}_2$  groups in the fragments discussed above, compatible with the  $\text{TFSI}_{\text{dec-1}}$  peaks in these ranges. The BE of 689.2 eV computed for the F 1s core level is close to that of the  $\text{CF}_3$  groups, e.g., in the TFSI anion and could not be distinguished. For the C 1s spectral range, however, the situation is different. The BE of 290.8 eV computed for the  $\text{CF}_2$  group is substantially lower than that of the  $\text{CF}_3$  groups (293.1–293.5 eV), and since there also no new peaks appearing in this energy range the formation of measurable amounts of the  $\text{LiN}(\text{CF}_2)(\text{SO}_2)$  intermediate can be ruled out.

Next, also decomposition products such as  $\text{LiSO}_2\text{CF}_3$  or  $\text{LiSO}_2\text{F}$  show O 1s BEs of 532.6 eV and 531.6 eV, respectively, which might explain the emerging  $O_{\text{TFSI,dec-1}}$  peak at 532.0 eV as well. For  $\text{LiSO}_2\text{CF}_3$  the C 1s and F 1s BEs would be in the typical range of  $\text{CF}_3$  groups (292.2, 688.9 eV), though slightly lower than in the previous cases. Nevertheless, contributions from these intermediates could not be excluded based on these signals. The same is finally true also for the S 2p signal, where the computed BE (166.9 eV) could be included on the low-BE side of the  $S_{\text{TFSI,dec-1}}$  peak (yellow peak in Figure 2). For  $\text{LiSO}_2\text{F}$  the resulting F 1s peak (computed BE: 685.0 eV) would appear in the range of the new  $F_{\text{TFSI,dec-1}}$  peak (yellow peak in Figure 2), while the S 2p signal (computed BE: 166.3 eV) would be close to values calculated for  $\text{SO}_2$  groups (see above), but significantly lower than the  $S_{\text{TFSI,dec-1}}$  peak observed experimentally. Thus, as stated before, the formation of  $\text{LiSO}_2\text{F}$  as reaction intermediate is less probable, unless there is a considerable deviation in the calculated S 2p BE.

Finally, looking at the decomposition of the BMP cation, the ring opening process has been identified as the most probable initial reduction step (see Table 2). The computed N 1s BE of the resulting BMP radical ( $\cdot\text{NC}_9\text{H}_{20}$ ) is about 400.1 eV (see Table 4), which is in excellent agreement with the experimental BE ( $N_{\text{BMP,dec-1}}$  green peak in Figure 1). However, due to its high

**Table 6.** Calculated and experimental<sup>[28,78,79]</sup> N 1s, O 1s, F 1s or S 2p BEs (in eV) of different inorganic Li salts given with respect to the valence band maximum.

	calculated	experimental	
$\text{Li}_3\text{N}$	394.2	394.0	Ref. [28]
$\text{Li}_2\text{O}$	527.6	526.5	Ref. [28]
$\text{Li}_2\text{O}_2$	528.4	530.8	Ref. [28]
$\text{Li}_2\text{CO}_3$	528.6	528.9	Ref. [28]
$\text{LiF}$	680.7	679.8	Ref. [78]
$\text{Li}_2\text{S}$	158.9	159.2	Ref. [79]

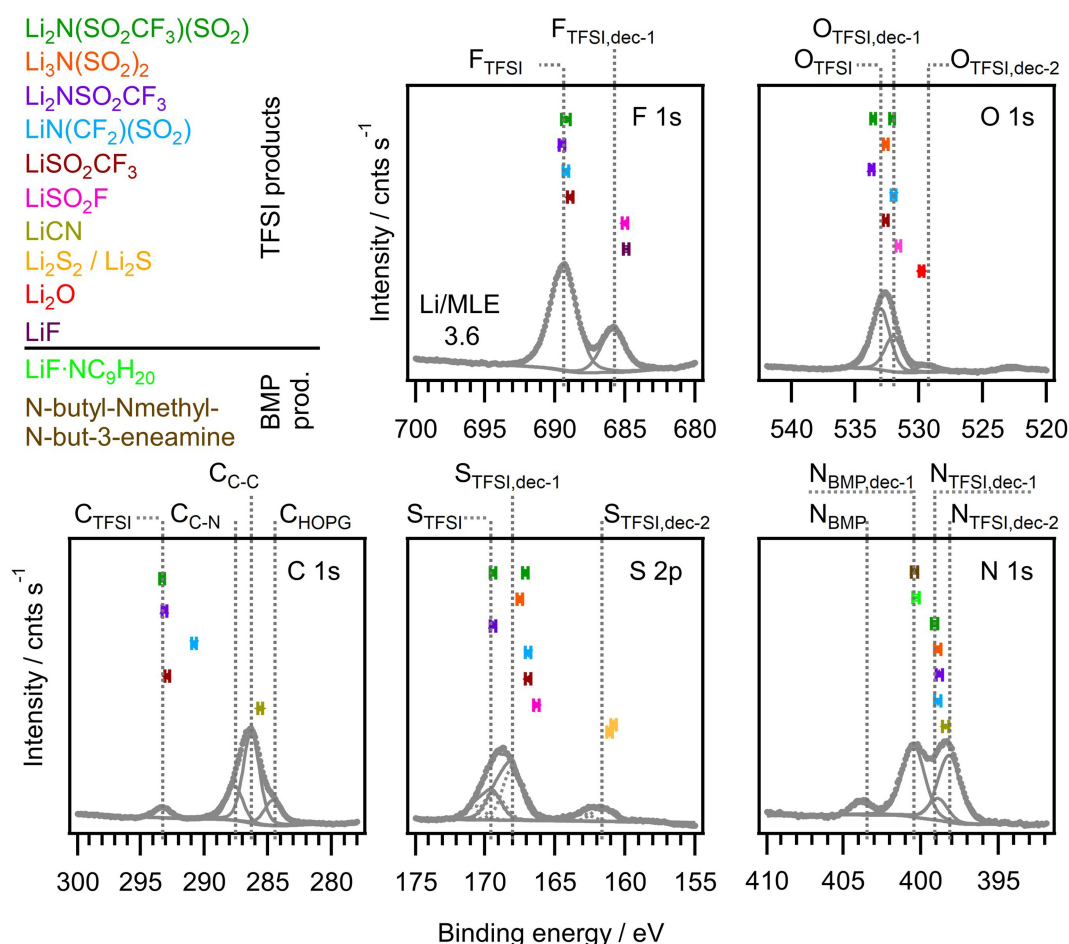
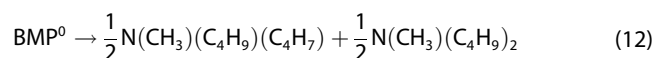


**Figure 7.** F 1s, O 1s, C 1s, S 2p and N 1s core level spectra of an adsorbed BMP-TFSI multilayer (~10 ML) after post-deposition 3.6 ML Li (bottom of each panel). The calculated BEs of several fragments are inserted as markers in the panels (error bar  $\pm 0.2$  eV).

reactivity, the radical presumably will not persist as observable intermediate and is prone to subsequent reactions. As discussed above, by abstraction of an H-atom or other intermolecular reactions tertiary amines will result. They show computed N 1s BEs of 400.4 or 400.9 eV, that are well in the range of the experimentally observed broad peak ( $N_{\text{BMP,dec-1}}$ ). Though further reductions of the obtained amines to amides cannot be excluded energetically, their formation is not unambiguously favored. On the other hand, the N 1s BE computed for lithium butylmethanamide (399.0 eV, see Table 4) is much lower than the experimental peak assigned to BMP decomposition products at around 400 eV. Hence, amide products are presumably not formed. Possible pyrrolidine products, in contrast, reveal significantly higher N 1s BEs of around 402 eV (Table 4). Based on the experimental spectra, their formation is therefore unlikely as well. The same is also true for the formation of  $\text{Li}_3\text{N}$ , which was excluded already before as a reaction product for the reaction between Li and TFSI, based on the absence of a peak in the range around 395 eV, where the N 1s BE was reported<sup>[28]</sup> and also calculated (Table 5). Furthermore, we did not consider the possibility that LiCN is formed as decomposition product of BMP, as the

cleavage of more than two N–C bonds of BMP is energetically not favored.

In total, reactions of the BMP cation and Li lead most likely to the formation of tertiary amines due to subsequent reactions of radicals resulting from one electron reductions:



## Conclusion

Aiming at a detailed insight into the mechanisms and initial products of the SEI formation in Li ion batteries, we have studied the reaction of BMP-TFSI and Li by employing XPS measurements and DFT-based calculations. Combining the results of the experiments and calculations, the following conclusions can be drawn:

- Initially, mainly the TFSI anion is reduced by reaction with Li atoms. Thereby, either the S–C or the N–S bond is cleaved, leading to almost isoenergetic products:  $\text{LiN}(\text{SO}_2\text{CF}_3)(\text{SO}_2)$  or  $\text{Li}_3\text{N}(\text{SO}_2)_2$  and  $\text{Li}_2\text{NSO}_2\text{CF}_3$ . Besides, volatile fluorinated hydrocarbons (e.g.  $\text{C}_2\text{F}_4$ ) are formed according to Eqs. 9–10.

- Lithium cyanamide or cyanide is found as energetically stable product in a Li-poor regime (see section Thermodynamic stability of possible reaction products of BMP-TFSI and  $\text{Li}^0$ ), yet its formation is hindered by an energetic barrier  $E^{\ddagger}$  (see section Kinetic stability of intermediate products of the reaction of  $\text{TFSI}^-$  and  $\text{Li}^0$  and Eq. 11). The reaction barrier of its formation declines considerably with increasing Li concentration.
- At larger amounts of Li, BMP is reduced as well. A ring opening reaction has been identified as the most likely one-electron reduction mechanism. Yet, stabilization of the resulting radicals by subsequent reactions with neighboring radicals might lead to products comparable to the products of a Hofmann-elimination (see Eq. 12).
- Only at a chemical potential of Li that is close to the chemical potential of metallic Li,  $\text{Li}_3\text{N}$  is found as possible product. This implies that in electrochemical studies varying the electrode potentials not lower than 0.5 V vs  $\text{Li}/\text{Li}^+$ , but low enough to enable electrolyte decomposition,  $\text{Li}_3\text{N}$  might not occur as component in the initial SEI.
- The Li-induced reduction of BMP-TFSI on HOPG is different for monolayer and multilayer coverages of the IL. In the monolayer regime there seems to be a more selective reduction of TFSI, presumably due to the fact that the surface acts as electron acceptor and  $\text{HOPG}^{\delta-}-\text{Li}^{\delta+}-\text{TFSI}^{\delta-}$  structures are formed as intermediates,<sup>[15]</sup> while BMP is stabilized via interactions with the partially negatively charged substrate. In the multilayer regime BMP is reduced as well, leading to a neutral BMP decomposition product, in which the N 1s electron has a BE similar to that of the N 1s electron in TFSI. Furthermore, we did not find a specific desorption of N-containing products in the multilayer regime that would lead to a modification in the measured N-content of the film.

Overall, we have shown that combined calculational and experimental studies of well defined model systems can provide detailed, molecular scale insights into the complex electrolyte decomposition reactions and the composition of the products, which is a prerequisite for the systematic knowledge-based development of electrolytes with tailored stabilities and decomposition patterns that are indispensable for an improved battery performance.

## Methods

### Experiment

The experiments were carried out in a commercial UHV system (SPECS) with a base pressure of  $2 \times 10^{-10}$  mbar. It consists of two chambers, one containing an Aarhus-type STM/AFM system (SPECS Aarhus SPM150 with a Colibri sensor), the other one is equipped with an X-ray source (SPECS XR50, Al- $K_{\alpha}$  and Mg- $K_{\alpha}$ ), a He lamp (SPECS UVS 300) and a hemispherical analyzer (SPECS, DLSEGD-Phoibos-Has3500) for XPS and UPS measurements. The highly oriented pyrolytic graphite(0001) (HOPG) single crystal was purchased from MaTeck (ZYA, mosaic spread  $0.4^\circ \pm 0.1^\circ$ ), exhibiting a cuboid shape with a size of  $10 \text{ mm} \times 10 \text{ mm} \times < 1 \text{ mm}$ . The HOPG sample was fixed on a tantalum sample plate with silver conductive

paste, and then heated in a  $\text{N}_2$  flooded oven for 30 minutes at 723 K to degas the conductive silver paste. The HOPG surface was cleaned by removing graphene layers with a tape and subsequently transferred into the load lock of the UHV system. Finally, it was moved into the UHV chamber via a linear transfer, where it was flashed to  $\sim 600 \text{ K}$ , which results in a clean HOPG surface. The ionic liquid (IL) 1-butyl-1-methylpyrrolidinium bis(trifluoromethylsulfonyl)imide (BMP-TFSI) was filled into a quartz crucible which was mounted in a Knudsen effusion cell (Ventiotec, OVD-3). Prior to its use, the IL was carefully degassed in UHV at around 400 K for 24 h to obtain a pure, water-free IL. To generate IL adlayers on the graphite(0001) surface, we evaporated the IL at a temperature of the IL source of 450 K. Under these conditions, the deposition rate was  $\sim 0.1 \text{ ML min}^{-1}$ , with 1 monolayer (ML) defined as a layer at saturation coverage. Lithium metal was deposited from an alkali getter source (SAES Getters), by resistively heating the source (7.1 A, 1.1 V) in line-of-sight of the sample at a distance of around 6 cm. Deposition rates of approximately  $0.04\text{--}0.05 \text{ MLE min}^{-1}$  (monolayer equivalents) were calculated from the damping of the C 1s substrate peak after successive vapor deposition of Li at 80 K, where intercalation and bulk dissolution, e.g., via defects, are inhibited. For the evaluation we assume that a ML Li has a thickness  $d$  of  $2.48 \text{ \AA}$ , equivalent to the (110) interplanar distance in a body centered cubic lattice (the stable configuration of Li metal at r.t.). The layer thickness  $d$  was calculated by  $I_d = I_0 \exp(-d/\lambda \cos \theta)$ , with an electron inelastic mean free path (IMFP)  $\lambda$  of  $46 \text{ \AA}$ <sup>[46]</sup> for electrons with a kinetic energy of  $\sim 1200 \text{ eV}$  in Li. For the XPS measurements we used an Al- $K_{\alpha}$  X-ray source (1486.6 eV), operated at a power of 250 W ( $U = 14 \text{ kV}$ ,  $I = 17.8 \text{ mA}$ ). XP spectra were recorded at a pass energy  $E_{\text{pass}}$  of 100 eV at grazing emission (80 to the surface normal, surface sensitive mode, information depth of 1–2 nm). Shifts due to sample charging could be excluded. Peak fitting was performed using the Igor pro 8.04 software; all peaks were fitted with a simultaneous fit of the background (Shirley + slope) and of the signal. Here we assumed a pseudo-Voigt type peak shape, which is a linear combination of a Gaussian and a Lorentzian function.

### Computation

The Vienna ab initio simulation package (VASP 5.4)<sup>[47,48]</sup> was used to perform periodic density functional theory calculations of BMP-TFSI and possible products of its reaction with Li. The electronic wave functions were expanded in a plane wave basis set up to a cutoff energy of 520 eV and the ionic cores were described by the projector augmented wave (PAW) method.<sup>[49,50]</sup> Exchange-correlation energies were evaluated within the generalized gradient approximation (GGA), employing a revised version of the Perdew-Burke-Ernzerhof functional (RPBE).<sup>[51]</sup> Dispersion effects were accounted for by the semi-empirical correction scheme of Grimme (D3)<sup>[52]</sup> in connection with a damping function proposed by Chai and Head-Gordon (zero-damping).<sup>[53]</sup> As shown before, this method yields a reliable description both of the lattice parameters of BMP-TFSI<sup>[18]</sup> and also of the interaction energy of this and similar ion pairs,<sup>[54]</sup> at least as long as equilibrium inter-fragment distances of the ion pairs are employed.<sup>[55]</sup>

We restricted the set of possible products of Eq. 1 to known organic or inorganic Li salts or compounds consisting of elements present either in BMP or TFSI. In detail, we employed experimentally available crystal structures of lithium oxide,<sup>[56]</sup> peroxide,<sup>[57]</sup> sulfide,<sup>[56]</sup> (fluoro)sulfate,<sup>[58,59]</sup> trifluoromethanesulfonate,<sup>[60]</sup> carbonate,<sup>[61]</sup> carbide,<sup>[62]</sup> cyanide,<sup>[63]</sup> cyanamide,<sup>[64]</sup> nitride<sup>[65]</sup> and fluoride<sup>[66]</sup> as input structures for geometry optimizations. Input structures of lithium sulfite and dithionite were adopted from known crystal structures of the respective sodium compounds.<sup>[67,68]</sup>



Mixed lithium oxide / lithium sulfide structures, such as  $\text{Li}_2\text{SO}_2$  and  $\text{Li}_2\text{SO}$ , were considered as well. A crystalline structure of trilithium-trisulfimide ( $\text{LiNSO}_2$ ) was calculated adopting the crystal structure of triammonium-trisulf-imide<sup>[69]</sup> and the further reduced  $\text{LiNSO}$  was considered based on the crystal structure of the related tetramethylammoniumthionylimide.<sup>[70]</sup> Larger fragments of TFSI such as  $\text{Li}_2\text{NSO}_2\text{CF}_3$ ,  $\text{Li}_2\text{N}(\text{CF}_3)(\text{SO}_2)$ ,  $\text{LiN}(\text{CF}_2)(\text{SO}_2)$ ,  $\text{LiNCF}_2$ ,  $\text{LiN}(\text{SO}_2)_2$ ,  $\text{Li}_3\text{N}(\text{SO}_2)_2$ ,  $\text{LiSO}_2\text{CF}_3$  and  $\text{LiSO}_2\text{F}$  were calculated assuming the space group P-1 with two molecules per unit cell, which has been reported for the structurally related compound trifluoromethanesulfonamide.<sup>[71]</sup> Calculations of  $\text{Li}_2\text{N}(\text{SO}_2\text{CF}_3)(\text{SO}_2\text{CF}_2)$  and  $\text{Li}_2\text{N}(\text{SO}_2\text{CF}_3)(\text{SO}_2)$  employed orthorhombic unit cells including four molecules similar to the unit cell of the experimentally determined crystal structure of BMP-TFSI.<sup>[72]</sup> For the reduction products of BMP, simple orthorhombic structures with one molecule per unit cell were used as input structure, accounting for the fact that linear alkanes or alkylamines with longer side chains adopt crystal structures in which the alkyl chains are packed in a parallel fashion.<sup>[73,74]</sup> Additional input structures for *N,N*-Dibutyl-*N*-methylamine and *N*-Butyl-*N*-methyl-*N*-but-3-eneamine were adopted from the crystal structure of dibutylamine,<sup>[74]</sup> which includes four molecules per unit cell. Besides the solid products, the possibility of gaseous products such as  $\text{CO}$ ,  $\text{CO}_2$ ,  $\text{SO}_2$ ,  $\text{F}_2$ ,  $\text{C}_2\text{F}_4$ ,  $\text{C}_2\text{F}_6$  was taken into account. Reduction products of BMP were not only calculated as crystalline structures, but also as isolated molecules. All isolated or gaseous products were modelled within a large box that allows a vacuum region of at least 15 Å between periodic images of the molecules. For the integration over the first Brillouin zone only the  $\Gamma$  point was employed for calculations of isolated molecules, whilst for crystalline bulk structures the number of  $\Gamma$  centered k-points was increased to between  $2 \times 2 \times 2$  and  $13 \times 13 \times 13$  k-points, depending on the size of the unit cell of the bulk structure and making sure that the k-point sets were well-converged. Lattice and geometry optimizations were carried out until all forces on atoms were less than 0.01 eV/Å. The electronic structure was converged within  $10^{-6}$  eV.

Furthermore, core level binding energies (BE) of BMP-TFSI and its reaction products with Li were determined. In general, the BE can be calculated according to Eq. (13)

$$\text{BE} = E_{N-1}^f - E_N^i + \mu \quad (13)$$

where  $E_{N-1}^f$  denotes the total energy of the final state, i.e., of the ionized system with one less core electron.  $E_N^i$  is the energy of the neutral initial state and  $\mu$  is the common chemical potential of the electrons of analyzer and sample.<sup>[75,76]</sup> Calculations of the ionized system within periodic boundary conditions would lead to a coulombic divergency unless further corrections are employed. Within the implementation for core level energy calculations in VASP,<sup>[77]</sup> calculations of the ionized system are circumvented by exciting the core electron (X) to the Fermi level in the valence band and thus retaining a charge neutral system with a total energy  $E_N^f(X)$ . Core levels energies X (X=N 1s, S 2p, C 1s, O 1s or F 1s) of crystalline bulk structures were determined according to

$$\text{BE}^{\text{calc}}(X) = E_N^f(X) - E_N^i - (\varepsilon_{\text{fermi}}(f(X)) - \varepsilon_{\text{fermi}}(i)) + n\Delta \quad (14)$$

where the difference of the Fermi energies of the final and the initial state ( $\varepsilon_{\text{fermi}}(f(X)) - \varepsilon_{\text{fermi}}(i)$ ) is introduced as correction. Here,  $\varepsilon_{\text{fermi}}$  denotes the valence band maximum as given by VASP. Additionally, a fraction  $n$  of the band gap  $\Delta$  accounts for the level alignment as explained in the next paragraph. Finally, to allow comparison with experiment, binding energies were calibrated using experimental BE values of intact TFSI as reference according to Eq. (15):

$$\text{BE}(X) = \text{BE}^{\text{calc}}(X) + \text{BE}^{\text{exp}}(X_{\text{TFSI}}) - \text{BE}^{\text{calc}}(X_{\text{TFSI}}) \quad (15)$$

The experimental reference binding energies  $\text{BE}^{\text{exp}}(X_{\text{TFSI}})$  were obtained by XPS measurements of adsorbed BMP-TFSI multilayer films on graphite (see Table 1). For the calculation of  $\text{BE}^{\text{calc}}(X_{\text{TFSI}})$  according to Eq. 14 we employed the crystalline structure of BMP-TFSI to model the multilayer film. Its Fermi level was assumed to be pinned at the conduction band of BMP-TFSI ( $n=1$  in Eq. (14)). This yields calculated BEs of inorganic lithium salts, that, when given with respect to the valence band maximum, compare reasonably well with experiment (see Table 6). A rather strong deviation of the calculated BE from experiment can be observed in case of some lithium salts with a large band gap ( $\text{Li}_2\text{O}$ ,  $\text{Li}_2\text{O}_2$  and  $\text{LiF}$ ). A similar discrepancy between experiment and calculation has also been observed for  $\text{BeO}$ .<sup>[80]</sup> The authors of that study explained the deviation by the failure of the GGA functional to describe the position the valence band accurately. On the other hand, typically, experimental BEs are given with respect to the Fermi level. Thus, in the following, calculated BEs of inorganic lithium salts or molecular products of the reduction of BMP-TFSI according to Eq. (14) are reported with respect to the Fermi level which is assumed to be in the middle of the band gap ( $n=1/2$  in Eq. (14)) for inorganic lithium salts ( $\text{Li}_x\text{Z}_y$ ,  $Z=\text{N},\text{O},\text{S},\text{F}$ ). For all other larger molecular fragments this is assumed to be at the conduction band minimum ( $n=1$  in Eq. (14)), i.e., at the same position as assumed for the educt. The different choices for  $n$  stem from the fact that a vacuum level alignment of BMP-TFSI or large decomposition fragments and the substrate is assumed, whilst a Fermi level alignment of adsorbates' and substrate's levels occurs for more strongly bound smaller inorganic compounds formed close to the substrate. Finally we note that the supercells of all DFT calculations of BEs correspond to a multiple of the unit cells of the crystal structures to minimize spurious interaction of periodically repeated core holes. In particular for small unit cells such as inorganic binary lithium salts the BE was obtained by extrapolating the results of increasingly large supercells up to  $3 \times 3 \times 3$  times the size of the primitive unit cell to the limit of an infinite supercell, as proposed by Kahk et al.<sup>[80]</sup>

Besides the periodic calculations using VASP, RPBE-D3 calculations of isolated TFSI<sup>-</sup>, its possible initial reaction products with one or two Li atoms and kinetic barriers of intramolecular rearrangement processes of initial reaction products were performed using the ORCA quantum chemistry code (version 4.2).<sup>[81,82]</sup> The minimal augmented basis set def2-QZVPP of Ahlrichs et al.<sup>[83,84]</sup> was employed to expand the molecular electronic wave function. In order to account for the environment of the ionic liquid, the conductor-like polarizable continuum model (CPCM)<sup>[85]</sup> was used, applying a dielectric constant of 12, which is well within the range of experimentally determined dielectric constants reported for BMP-TFSI (11.9–14.7).<sup>[86,87]</sup> In geometry optimizations convergence tolerance values were set to  $5 \times 10^{-6} E_h$  and  $3 \times 10^{-4} E_h/\text{bohr}$  for geometric steps and to  $10^{-8} E_h$  for electronic self consistent field (SCF) steps. Finally, activation energies of intramolecular rearrangement processes were extracted from minimum energy paths for the respective reaction, which were calculated by the climbing image nudged elastic band (NEB) method.<sup>[88,89]</sup>

## Acknowledgements

We gratefully acknowledge financial support from the German Research Foundation (DFG) under project ID 390874152 (POLiS Cluster of Excellence, EXC 2154) and computer time provided by the state of Baden-Württemberg through bwHPC and the DFG

through grant no. INST 40/575-1 FUGG (JUSTUS 2 cluster). The work contributes to the research performed at CELEST (Center for Electrochemical Energy Storage Ulm-Karlsruhe). Open Access funding enabled and organized by Projekt DEAL.

## Conflict of Interest

The authors declare no conflict of interest.

## Data Availability Statement

The data that support the findings of this study are available from the corresponding author upon reasonable request.

**Keywords:** density functional calculations · ionic liquids · lithium · photoelectron spectroscopy · solid electrolyte interphase

- [1] P. Verma, P. Maire, P. Novák, *Electrochim. Acta* **2010**, *55*, 6332.
- [2] M. Armand, F. Endres, D. R. MacFarlane, H. Ohno, B. Scrosati, *Nat. Mater.* **2009**, *8*, 621.
- [3] A. Lewandowski, A. Świdzka Mocek, *J. Power Sources* **2009**, *194*, 601.
- [4] B. Scrosati, J. Garche, *J. Power Sources* **2010**, *195*, 2419.
- [5] P. C. Howlett, E. I. Izgorodina, M. Forsyth, D. R. MacFarlane, *Z. Phys. Chem.* **2006**, *220*, 1483.
- [6] E. Markevich, R. Sharabi, V. Borgel, H. Gottlieb, G. Salitra, D. Aurbach, G. Semrau, M. A. Schmidt, *Electrochim. Acta* **2010**, *55*, 2687.
- [7] M. Tułodziecki, J.-M. Tarascon, P.-L. Taberna, C. Guéry, *Electrochem. Commun.* **2017**, *77*, 128.
- [8] Z. Liu, G. Li, A. Borodin, X. Liu, Y. Li, F. Endres, *J. Phys. Chem. C* **2019**, *123*, 10325.
- [9] M. Olschewski, R. Gustus, M. Marschewski, O. Höfft, F. Endres, *Phys. Chem. Chem. Phys.* **2014**, *16*, 25969.
- [10] M. Olschewski, R. Gustus, O. Höfft, A. Lahiri, F. Endres, *J. Phys. Chem. C* **2017**, *121*, 2675.
- [11] J. Kim, I. Weber, F. Buchner, J. Schnaidt, R. J. Behm, *J. Chem. Phys.* **2019**, *151*, 134704.
- [12] I. Weber, J. Kim, F. Buchner, J. Schnaidt, R. J. Behm, *ChemSusChem* **2020**, *13*, 2589.
- [13] F. Buchner, K. Forster-Tonigold, M. Bozorgchenani, A. Groß, R. J. Behm, *J. Phys. Chem. Lett.* **2016**, *7*, 226.
- [14] F. Buchner, J. Kim, C. Adler, M. Bozorgchenani, J. Bansmann, R. J. Behm, *J. Phys. Chem. Lett.* **2017**, *8*, 5804.
- [15] F. Buchner, K. Forster-Tonigold, J. Kim, C. Adler, J. Bansmann, A. Groß, R. J. Behm, *J. Phys. Chem. C* **2018**, *122*, 18968.
- [16] F. Buchner, B. Uhl, K. Forster-Tonigold, J. Bansmann, A. Groß, R. J. Behm, *J. Chem. Phys.* **2018**, *148*, 193821.
- [17] F. Buchner, K. Forster-Tonigold, J. Kim, J. Bansmann, A. Groß, R. J. Behm, *Chem. Mater.* **2019**, *31*, 5537.
- [18] K. Forster-Tonigold, J. Kim, J. Bansmann, A. Groß, F. Buchner, *ChemPhysChem* **2021**, *22*, 441.
- [19] L. E. Camacho-Forero, T. W. Smith, P. B. Balbuena, *J. Phys. Chem. C* **2017**, *121*, 182.
- [20] H. Yildirim, J. B. Haskins, C. W. Bauschlicher Jr, J. W. Lawson, *J. Phys. Chem. C* **2017**, *121*, 28214.
- [21] B. V. Merinov, S. V. Zybun, S. Naserifar, S. Morozov, J. Oppenheim, W. A. Goddard, J. Lee, J. H. Lee, H. E. Han, Y. C. Choi, S. H. Kim, *J. Phys. Chem. Lett.* **2019**, *10*, 4577.
- [22] H. S. Dhatarwal, Y.-W. Chen, J.-L. Kuo, H. K. Kashyap, *J. Phys. Chem. C* **2020**, *124*, 27495.
- [23] F. Buchner, K. Forster-Tonigold, T. Bolter, A. Rampf, J. Klein, A. Groß, R. J. Behm, *J. Vac. Sci. Technol. A* **2022**, *40*, 023204.
- [24] T. Cremer, M. Stark, A. Deyko, H.-P. Steinrück, F. Maier, *Langmuir* **2011**, *27*, 3662.
- [25] A. B. Biedron, E. L. Garfunkel, E. W. Castner Jr, S. Rangan, *J. Chem. Phys.* **2017**, *146*, 054704.
- [26] A. Jablonski, K. Wandelt, *Surf. Interface Anal.* **1991**, *17*, 611.
- [27] Y. Ge, T. Weidner, H. Ahn, J. E. Whitten, M. Zharnikov, *J. Phys. Chem. C* **2009**, *113*, 4575.
- [28] K. N. Wood, G. Teeter, *ACS Appl. Energ. Mater.* **2018**, *1*, 4493.
- [29] C. Xu, B. Sun, T. Gustafsson, K. Edström, D. Brandell, M. Hahlin, *J. Mater. Chem. A* **2014**, *2*, 7256.
- [30] D. Aurbach, A. Zaban, Y. Ein-Eli, I. Weissman, O. Chusid, B. Markovsky, M. Levi, E. Levi, A. Schechter, E. Granot, *J. Power Sources* **1997**, *68*, 91.
- [31] J. F. Moulder, W. F. Stickle, P. E. Sobol, K. D. Bomben, Handbook of X-ray photoelectron spectroscopy, (Ed.: J. Chastain), Perkin-Elmer Corp., Eden Prairie, MN 1992.
- [32] K. P. Yao, D. G. Kwabi, R. A. Quinlan, A. N. Mansour, A. Grimaud, Y.-L. Lee, Y.-C. Lu, Y. Shao-Horn, *J. Electrochem. Soc.* **2013**, *160*, A824.
- [33] S. Qiu, C. Lin, J. Chen, M. Strongin, *Phys. Rev. B* **1989**, *39*, 6194.
- [34] M. Helen, M. A. Reddy, T. Diemant, U. Golla-Schindler, R. J. Behm, U. Kaiser, M. Fichtner, *Sci. Rep.* **2015**, *5*, 1.
- [35] Y. Wu, T. Momma, S. Ahn, T. Yokoshima, H. Nara, T. Osaka, *J. Power Sources* **2017**, *366*, 65.
- [36] S. D. Ross, M. Finkelstein, R. C. Petersen, *J. Am. Chem. Soc.* **1960**, *82*, 1582.
- [37] C. E. Dahm, D. G. Peters, *J. Electroanal. Chem.* **1996**, *402*, 91.
- [38] M. C. Kroon, W. Buijs, C. J. Peters, G.-J. Witkamp, *Green Chem.* **2006**, *8*, 241.
- [39] Y. Preibisch, F. Horsthemke, M. Winter, S. Nowak, A. S. Best, *Chem. Mater.* **2020**, *32*, 2389.
- [40] J. F. Dohmann, F. Horsthemke, V. Küpers, S. Bloch, Y. Preibisch, A. Kolesnikov, M. Kolek, M. C. Stan, M. Winter, P. Bieker, *Adv. Energy Mater.* **2021**, *11*, 2101021.
- [41] A. Groß, S. Sakong, *Curr. Opin. Electrochem.* **2019**, *14*, 1.
- [42] J. K. Nørskov, J. Rossmeisl, A. Logadottir, L. Lindqvist, J. R. Kitchin, T. Bligaard, H. Jonsson, *J. Phys. Chem. B* **2004**, *108*, 17886.
- [43] K. S. Exner, *ChemSusChem* **2019**, *12*, 2330.
- [44] L. Suo, O. Borodin, T. Gao, M. Olguin, J. Ho, X. Fan, C. Luo, C. Wang, K. Xu, *Science* **2015**, *350*, 938.
- [45] Y. Liu, P. Yu, Y. Wu, H. Yang, M. Xie, L. Huai, W. A. Goddard III, T. Cheng, *J. Phys. Chem. Lett.* **2021**, *12*, 130.
- [46] C. Powell, A. Jablonski, NIST Electron Inelastic-Mean-Free-Path Database 71, Version 1.1 2000.
- [47] G. Kresse, J. Furthmüller, *Phys. Rev. B* **1996**, *54*, 11169.
- [48] G. Kresse, J. Furthmüller, *Comput. Mater. Sci.* **1996**, *6*, 15.
- [49] P. E. Blöchl, *Phys. Rev. B* **1994**, *50*, 17953.
- [50] G. Kresse, D. Joubert, *Phys. Rev. B* **1999**, *59*, 1758.
- [51] B. Hammer, L. B. Hansen, J. K. Nørskov, *Phys. Rev. B* **1999**, *59*, 7413.
- [52] S. Grimme, J. Antony, S. Ehrlich, H. Krieg, *J. Chem. Phys.* **2010**, *132*, 154104.
- [53] J.-D. Chai, M. Head-Gordon, *Phys. Chem. Chem. Phys.* **2008**, *10*, 6615.
- [54] M. Kim, T. Gould, E. I. Izgorodina, D. Rocca, S. Lebègue, *Phys. Chem. Chem. Phys.* **2021**, *23*, 25558.
- [55] S. Grimme, W. Hujo, B. Kirchner, *Phys. Chem. Chem. Phys.* **2012**, *14*, 4875.
- [56] E. Zintl, A. Harder, B. Dauth, *Z. Elektrochem. Angew. Phys. Chem.* **1934**, *40*, 588.
- [57] H. Föppl, *Z. Anorg. Allg. Chem.* **1957**, *291*, 12.
- [58] J. G. Albright, *Z. Kristallogr. – Cryst. Mater.* **1933**, *84*, 150.
- [59] Z. Žák, M. Kosička, *Acta Crystallogr. Sect. B* **1978**, *34*, 38.
- [60] M. Tremayne, P. Lightfoot, M. Mehta, P. Bruce, K. Harris, K. Shankland, C. Gilmore, G. Bricogne, *J. Solid State Chem.* **1992**, *100*, 191.
- [61] J. Zemmann, *Acta Crystallogr.* **1957**, *10*, 664.
- [62] R. Juza, V. Wehle, H.-U. Schuster, *Z. Anorg. Allg. Chem.* **1967**, *352*, 252.
- [63] J. A. Lely, J. M. Bijvoet, *Recl. Trav. Chim. Pays-Bas* **1942**, *61*, 244.
- [64] M. G. Down, M. J. Haley, P. Hubberstey, R. J. Pulham, A. E. Thunder, *J. Chem. Soc. Dalton Trans.* **1978**, pages 1407–1411.
- [65] A. Rabenau, H. Schulz, *J. Less-Common Met.* **1976**, *50*, 155.
- [66] H. Ott, *Z. Kristallogr. – Cryst. Mater.* **1926**, *63*, 222.
- [67] W. H. Zachariasen, H. E. Buckley, *Phys. Rev.* **1931**, *37*, 1295.
- [68] J. D. Dunitz, *Acta Crystallogr.* **1956**, *9*, 579.
- [69] C. Leben, M. Jansen, *Z. Naturforsch. B* **1999**, *54*, 757.
- [70] S. Mann, M. Jansen, *Z. Naturforsch. B* **1994**, *49*, 1503.
- [71] I. V. Sterkhova, B. A. Shainyan, *J. Phys. Org. Chem.* **2015**, *28*, 485.
- [72] A. R. Choudhury, N. Winterton, A. Steiner, A. I. Cooper, K. A. Johnson, *J. Am. Chem. Soc.* **2005**, *127*, 16792.
- [73] R. Boese, H.-C. Weiss, D. Bläser, *Angew. Chem. Int. Ed.* **1999**, *38*, 988.

- [74] F. Hanke, C. J. Pugh, E. F. Kay, J. B. Taylor, S. M. Todd, C. M. Robertson, B. J. Slater, A. Steiner, *Chem. Commun.* **2018**, 54, 6012.
- [75] T. Ozaki, C.-C. Lee, *Phys. Rev. Lett.* **2017**, 118, 026401.
- [76] M. Walter, M. Moseler, L. Pastewka, *Phys. Rev. B* **2016**, 94, 041112.
- [77] L. Köhler, G. Kresse, *Phys. Rev. B* **2004**, 70, 165405.
- [78] R. Schlaf, B. A. Parkinson, P. A. Lee, K. W. Nebesny, G. Jabbour, B. Kippelen, N. Peyghambarian, N. R. Armstrong, *J. Appl. Phys.* **1998**, 84, 6729.
- [79] M. Shek, T. Sham, J. Hrbek, G.-Q. Xu, *Appl. Surf. Sci.* **1991**, 48–49, 332.
- [80] J. M. Kahk, G. S. Michelitsch, R. J. Maurer, K. Reuter, J. Lischner, *J. Phys. Chem. Lett.* **2021**, 12, 9353.
- [81] F. Neese, *Wiley Interdiscip. Rev.: Comput. Mol. Sci.* **2012**, 2, 73.
- [82] F. Neese, *Wiley Interdiscip. Rev.: Comput. Mol. Sci.* **2018**, 8, e1327.
- [83] F. Weigend, R. Ahlrichs, *Phys. Chem. Chem. Phys.* **2005**, 7, 3297.
- [84] J. Zheng, X. Xu, D. Truhlar, *Theor. Chem. Acc.* **2011**, 128, 295.
- [85] V. Barone, M. Cossi, *J. Phys. Chem. A* **1998**, 102, 1995.
- [86] H. Weingärtner, *Z. Phys. Chem.* **2006**, 220, 1395.
- [87] M.-M. Huang, Y. Jiang, P. Sasisanker, G. W. Driver, H. Weingärtner, *J. Chem. Eng. Data* **2011**, 56, 1494.
- [88] V. Ásgeirsson, B. O. Birgisson, R. Bjornsson, U. Becker, F. Neese, C. Riplinger, H. Jónsson, *J. Chem. Theory Comput.* **2021**, 17, 4929.
- [89] G. Henkelman, B. P. Uberuaga, H. Jónsson, *J. Chem. Phys.* **2000**, 113, 9901.

---

Manuscript received: July 5, 2022

Revised manuscript received: August 21, 2022

Accepted manuscript online: September 5, 2022

Version of record online: October 6, 2022